

Geophysical Research Letters[®]

RESEARCH LETTER

10.1029/2022GL101320

Key Points:

- We show using force-balance modeling that a megathrust earthquake stress drop can trigger forearc-wide aftershock seismicity
- Model results explain the Tohoku earthquake aftershock distribution and reveal spatial variability in forearc stress and strength
- Most aftershocks occurred in areas that experienced an increase in deviatoric stress

Supporting Information:

Supporting Information may be found in the online version of this article.

Correspondence to:

A. Dielförder,
dielforder@geowi.uni-hannover.de

Citation:

Dielförder, A., Bocchini, G. M., Kemna, K., Hampel, A., Harrington, R. M., & Oncken, O. (2023). Megathrust stress drop as trigger of aftershock seismicity: Insights from the 2011 Tohoku earthquake, Japan. *Geophysical Research Letters*, 50, e2022GL101320. <https://doi.org/10.1029/2022GL101320>

Received 4 NOV 2022

Accepted 21 JAN 2023

Author Contributions:

Conceptualization: A. Dielförder, G. M. Bocchini

Investigation: A. Dielförder, G. M. Bocchini, K. Kemna, A. Hampel, R. M. Harrington, O. Oncken

Methodology: A. Dielförder, G. M. Bocchini, K. Kemna, A. Hampel, R. M. Harrington

Visualization: A. Dielförder, G. M. Bocchini






Writing – original draft: A. Dielförder, G. M. Bocchini

Writing – review & editing: A. Dielförder, G. M. Bocchini, A. Hampel, R. M. Harrington, O. Oncken

© 2023. The Authors.

This is an open access article under the terms of the [Creative Commons Attribution License](#), which permits use, distribution and reproduction in any medium, provided the original work is properly cited.

Megathrust Stress Drop as Trigger of Aftershock Seismicity: Insights From the 2011 Tohoku Earthquake, Japan

A. Dielförder¹ , G. M. Bocchini² , K. Kemna² , A. Hampel¹ , R. M. Harrington², and O. Oncken³ 

¹Institut für Geologie, Leibniz Universität Hannover, Hanover, Germany, ²Institut für Geologie, Mineralogie und Geophysik, Ruhr-Universität Bochum, Bochum, Germany, ³GFZ Deutsches GeoForschungsZentrum Potsdam, Potsdam, Germany

Abstract Numerous normal-faulting aftershocks in subduction forearcs commonly follow large megathrust earthquakes. Postseismic normal faulting has been explained by stress changes induced by the stress drop along the megathrust. However, details of forearc stress changes and aftershock triggering mechanisms remain poorly understood. Here, we use numerical force-balance models combined with Coulomb failure analysis to show that the megathrust stress drop supports normal faulting, but that forearc-wide aftershock triggering is feasible within a narrow range of megathrust stress drop values and preseismic stress states only. We determine this range for the 2011 Tohoku earthquake (Japan) and show that the associated stress changes explain the aftershock seismicity in unprecedented detail and are consistent with the stress released by forearc seismicity before and after the earthquake.

Plain Language Summary Earthquakes release stresses that build up in the Earth due to the motion of tectonic plates. The stress release can cause additional earthquakes called aftershocks. Several thousand onshore and offshore aftershocks followed the great Tohoku subduction earthquake in March 2011. Whether the stress release of the Tohoku earthquake triggered most of the aftershocks is not well understood, because it is largely unknown how the stress field changed following the earthquake. We therefore use a computer model to estimate the stress release and resulting stress change required to explain the aftershock distribution. We find that 78% of the aftershocks occurred in areas where the Tohoku earthquake caused a subsequent stress increase. Our model results are further consistent with the stress release of smaller earthquakes that occurred in Japan before and after the Tohoku earthquake. Our findings provide new insights into aftershock triggering and help to understand where aftershocks occur after great earthquakes at subduction zones.

1. Introduction

Seismological records indicate that seismicity in forearcs increases after large megathrust earthquakes (Dewey et al., 2007; Hasegawa et al., 2012; Lange et al., 2012). Aftershock seismicity often shows a complex spatial distribution, is highest in the first weeks after the megathrust event, and decays at a power-law like rate (“Omori’s law,” Parsons, 2002; Toda & Stein, 2022), as exemplified by the 11 March 2011 M_w 9.0 Tohoku earthquake, Japan (Figure 1). The low forearc seismicity in the years before the earthquake focused near the plate interface and volcanic arc (Figures 1a and 1c). Seismicity immediately after the earthquake increased and spread throughout the forearc (Figures 1b and 1d). Seismicity rates were highest in the month following the Tohoku earthquake and decreased rapidly afterward (Figure 1e). The seismicity rate at the end of 2011 decreased by ~95%, but was still higher than before the Tohoku earthquake.

The increase in forearc seismicity indicates that the stress change caused by the megathrust earthquake destabilized the forearc. The exact causes and magnitude of this stress change remain uncertain, although seismological records provide important information on changes in forearc stress. Forearc seismicity after the Tohoku earthquake was dominated by normal faulting (Figure 1d), despite the thrust mechanism of the main shock and prevalence of reverse and strike-slip faulting in the decades preceding it (Hardebeck, 2012; Hasegawa et al., 2012; Yoshida et al., 2012). The normal faulting indicates that the stress state switched from deviatoric compression to deviatoric tension due to the Tohoku earthquake. The stress reversal only occurred in the offshore forearc and coastal regions near Iwaki. Reverse and strike-slip faulting continued inland Japan (Figure 1; Yoshida et al., 2019). Previous studies also inferred similar stress reversals for other megathrust earthquakes, including the 2004 M_w 9.1 Sumatra and 2010 M_w 8.8 Maule earthquakes (Hardebeck, 2012).

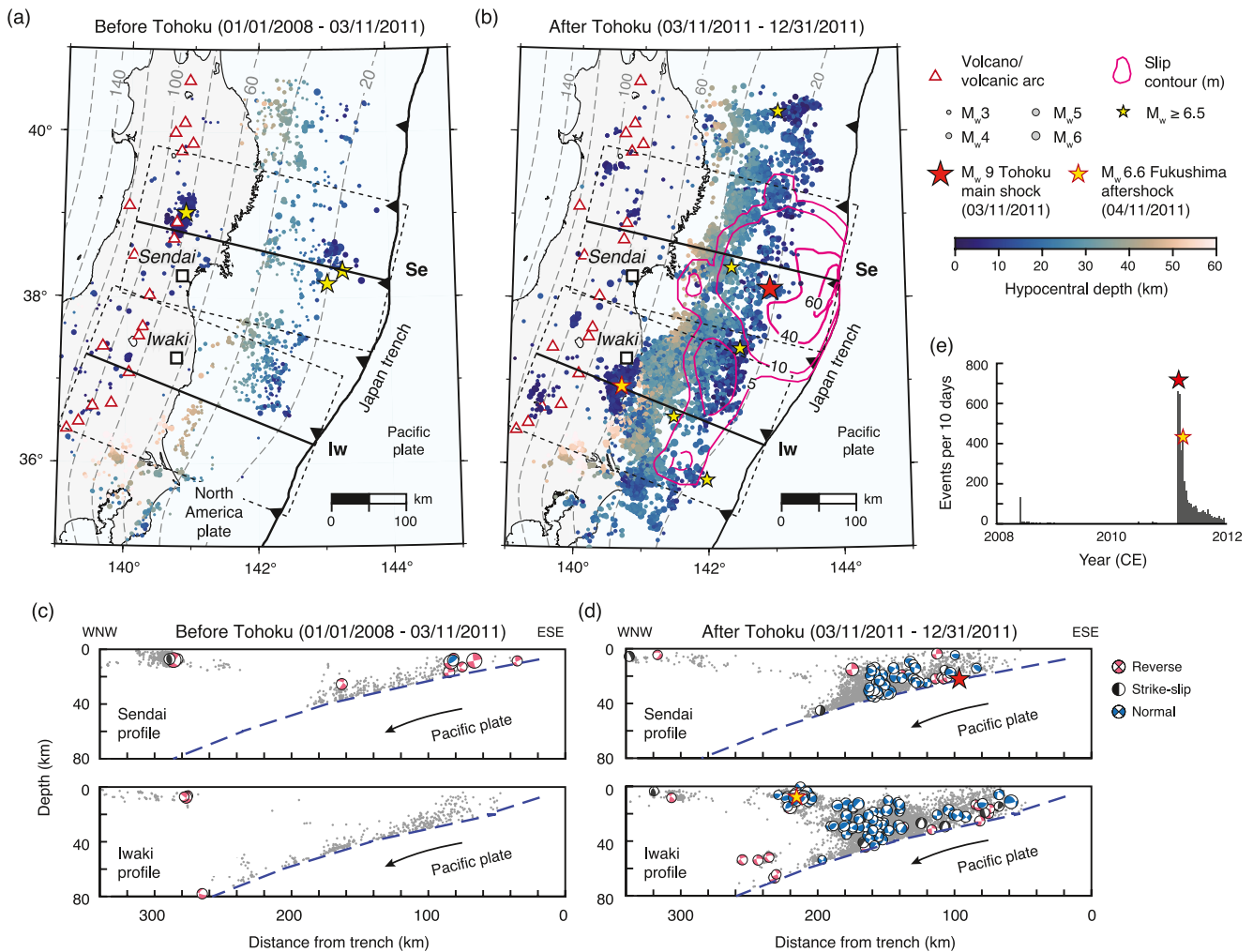


Figure 1. Seismotectonic setting of NE Japan. (a–d) Forearc seismicity before and after the Tohoku earthquake. (a, b) Map view. Black lines indicate location of cross-sections shown in (c) and (d). Dashed rectangles indicate the width of swaths (200 km) projected into the cross-sections. Se = Sendai, Iw = Iwaki. (c, d) Cross-sectional view. Gray dots are aftershock hypocenters from the Japan Meteorological Agency (JMA). Beach balls denote JMA focal mechanism solutions and are shown in profile view. Reverse faulting events in the outer marine forearc above the megathrust are likely poorly located interplate events (Nakamura et al., 2016) or the slab model is not accurate enough to classify them as interplate events. (e) Number of forearc earthquakes. Count includes events with magnitude \geq magnitude of completeness ($M_c = 3.4$, Text S3 in Supporting Information S1).

Previous work explained the stress reversal to result from the stress drop of the megathrust earthquake, i.e., the coseismic decrease in megathrust shear stress due to fault weakening processes (Di Toro et al., 2011; Hardebeck, 2012; Hasegawa et al., 2011; Scholz, 1998). The megathrust shear stress loading in the interseismic period causes compression of the forearc (Lamb, 2006; Wang & He, 1999), without which the forearc would experience deviatoric tension due to gravitational stresses resulting from density contrasts and margin topography. If the megathrust shear stress decreases during an earthquake, the loss in compression can cause a reversal from deviatoric compression to deviatoric tension and trigger normal faulting in the forearc (Cubas et al., 2013; Dielforder, 2017; Wang et al., 2019). However, the detailed stress changes caused by the stress drop of megathrust earthquakes like Tohoku remain unresolved. Consequently, it is unknown whether the stress change can explain the broad aftershock seismicity in the forearc.

Aftershock seismicity of megathrust earthquakes has been further investigated by Coulomb failure stress (CFS) models, which test whether the resulting stress changes of an earthquake promote or suppress failure on neighboring faults (Fariás et al., 2011; Terakawa et al., 2013; Toda et al., 2011). CFS models for the Tohoku earthquake showed that the stress change promoted some of the aftershocks and likely increased forearc seismicity rates. Aftershock seismicity not promoted by the stress change was interpreted to have been triggered either by

an increase in fluid pressure (Terakawa et al., 2013) or the presence of small faults of variable orientation (Toda et al., 2011). CFS models commonly determine the stress change in the forearc solely from the earthquake slip distribution and neglect the total stresses in the forearc resulting from gravitational and megathrust shear stresses. The total stresses determine, however, the forearc stress state (i.e., the magnitude and orientation of principal stresses) and we show in Section 2 that the preseismic stress state affects the stress change in the forearc that results from a stress drop on the megathrust. Thus, assessing whether a megathrust stress drop supports or inhibits failure in the forearc requires detailed information on the preseismic or postseismic stress state.

For Japan, estimates of the megathrust stress drop and preseismic and postseismic stress states exist (Brodsky et al., 2020; Brown et al., 2015; Wang et al., 2019; Yang et al., 2013), but the available data do not allow an unambiguous assessment of forearc stress changes. We therefore pursue an innovative modeling approach that determines the preseismic and postseismic stress states and related stress change compatible with broad aftershock triggering due to the megathrust stress drop. Using the aftershock distribution and fault kinematics as modeling constraints allows determining the precise stress conditions required for triggering the bulk forearc seismicity that occurred in the first months after the Tohoku earthquake. The model results are supported by independent stress drop observations.

2. Modeling Approach

We use a plane-strain finite-element model of force balance following Wang et al. (2019) to assess the stress change caused by the megathrust stress drop. The model is created with the software ABAQUS and comprises a rigid lower plate in frictional contact with an elastic upper plate representing the forearc (Figure 2a, Text S1 and Figure S1 in Supporting Information S1). ABAQUS computes the total stress tensor in the upper plate resulting from all applied boundary conditions, including gravity, isostasy, and friction along the plate contact (megathrust). We compute gravitational stresses for average densities of 2,800 and 3,300 kg m⁻³ for crustal and mantle parts, respectively, and seawater load using a density of 1,025 kg m⁻³. Gravitational acceleration is 9.81 m s⁻¹. Friction along the megathrust is generated by displacing the lower plate and computed for the effective friction coefficient μ' assigned to the megathrust, such that the megathrust shear stress τ is given by standard Coulomb friction ($\tau = \mu' \sigma_n$, where σ_n is normal stress).

To simulate the megathrust stress drop, the finite-element model includes a preseismic and a postseismic model step between which τ changes. The two model steps describe the stress state shortly before and after the megathrust earthquake, but not the stress state averaged over multiple earthquake cycles as in other force-balance applications (Dielforder & Hampel, 2021; Lamb, 2006). Because τ also increases during earthquakes, e.g., due to fault strengthening processes downdip of the main rupture zone (Brown et al., 2015; Scholz, 1998), we divide the megathrust into fault weakening and fault strengthening segments (Figure 2a). The model implements weakening and strengthening behavior by decreasing and increasing the μ' values of fault segments between the preseismic and postseismic model steps, respectively. Because μ' is adjusted manually, the model does not involve a rate-and-state friction law and the results are independent of slip rate. As such, we do not model the coseismic stress evolution as in seismic cycle models (Sobolev & Muldashev, 2017; van Zelst et al., 2019).

To determine the forearc stress change as function of the preseismic and postseismic stress states, we solve the model for different pairs of preseismic and postseismic μ' values. We then determine the megathrust stress drop and resultant forearc stress change as difference in megathrust shear stress and forearc stress between the postseismic and preseismic model steps, respectively. Finally, we determine whether the stress change brings the forearc closer to or further from Coulomb failure in each model run. To do so, we first calculate the critical friction coefficient μ_c , for which faults in the forearc were critically stressed at the given stresses. Note that μ_c is calculated from the preseismic and postseismic model solutions using the Coulomb criterium for a cohesionless fault and is not a model input parameter (Text S2 in Supporting Information S1). If μ_c increases from the preseismic to the postseismic model step, the postseismic stresses support failure on stronger faults, which is compatible with an increase in seismicity after a megathrust earthquake. Conversely, if μ_c decreases, the stress change inhibits failure and seismicity and is incompatible with a seismicity increase. Accordingly, we can define the failure tendency $\Lambda = (\mu_{c,\text{post}} - \mu_{c,\text{pre}})/\mu_{c,\text{pre}}$ to describe whether the stress change supports ($\Lambda > 0$) or inhibits failure ($\Lambda < 0$).

Figure 2b illustrates the stress state in the forearc as function of μ' for an exemplary point in the outer forearc. The calculations were carried out for a generic forearc setup and varying μ' uniformly along the megathrust (Text S1

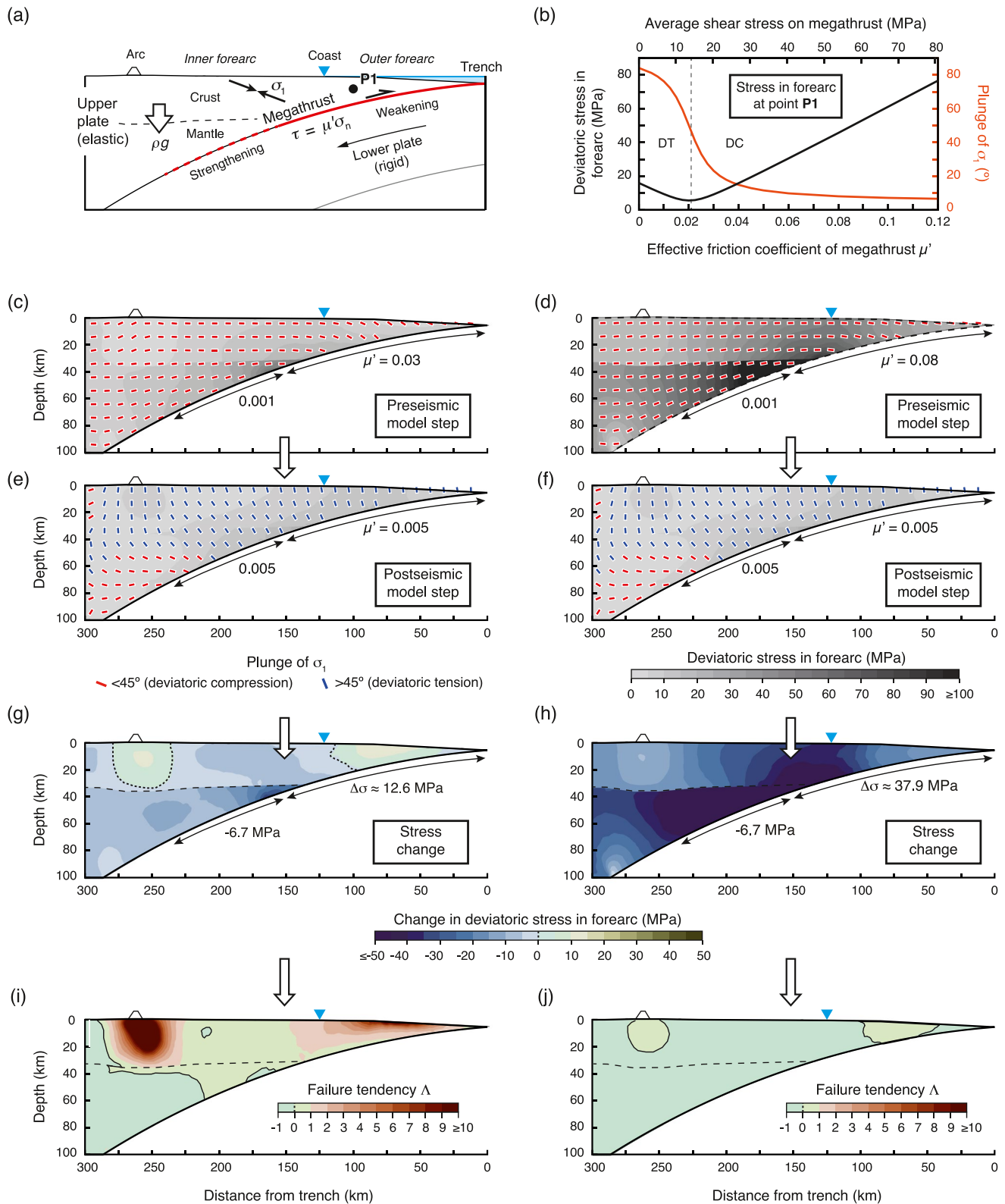


Figure 2. Model setup and generic models results. (a) Schematic representation of forearc model. Here, ρ is density, g is gravitational acceleration, μ' is the megathrust effective friction coefficient, τ and σ_n are the shear and normal stresses, respectively, and σ_1 is maximum compressive stress. (b) Deviatoric stress σ_{dev} (black) and plunge of σ_1 (orange) as function of μ' and average megathrust shear stress. Solutions are for site P1 in (a). DT and DC denote deviatoric tension and deviatoric compression, respectively. (c–f) Model results. (c–f) Deviatoric stress and plunge of σ_1 for preseismic and postseismic model steps. (g, h) Change in σ_{dev} due to megathrust stress drop $\Delta\sigma$. Positive and negative values of $\Delta\sigma$ indicate decrease and increase in megathrust shear stress, respectively. (i, j) Failure tendency Λ .

in Supporting Information S1). If μ' approaches zero, gravitational stresses dominate and the forearc experiences deviatoric tension (plunge of maximum compressive stress $\sigma_1 > 45^\circ$). Conversely, as μ' increases, megathrust shear stresses dominate and the forearc experiences deviatoric compression (plunge of $\sigma_1 < 45^\circ$). Note that for common μ' values of ≤ 0.06 (Gao & Wang, 2014) the deviatoric stress in the forearc and plunge of σ_1 do not vary linearly with μ' due to the opposing effect of gravitational and megathrust shear stresses on the stress field (Figure 2b). Thus, the stress change in the forearc and final stress state resulting from a change in τ depend on the initial megathrust shear stress (Figure S2 in Supporting Information S1). For example, a decrease in τ of 10 MPa from 35 to 25 MPa decreases the deviatoric stress by ~ 11 MPa while the stress state remains compressive. For comparison, a decrease in τ from 15 to 5 MPa increases the deviatoric by ~ 5 MPa but the stress state switches from deviatoric compression to tension (Figure 2b).

Figures 2c–2j illustrates for the generic forearc model that the failure tendency varies substantially with the preseismic stress state, even if the postseismic stress state is identical (note that μ' differs for the strengthening and weakening segments in these model runs). If the megathrust shear stress and forearc stress are low before the earthquake (Figure 2c), Λ increases in most of the forearc (Figure 2i). The increase in Λ results from two effects: first, the stress drop results in a reversal in the stress state from deviatoric compression to deviatoric tension, which supports failure because normal faulting operates at lower stresses than reverse faulting (Sibson, 1998). Second, the decrease in horizontal compression results in a net stress increase due to gravitational effects in areas of steep topography, such as the outer forearc (Figure 2g). For comparison, if the megathrust shear stress and forearc stresses are higher before the earthquake (Figure 2d), then the stress drop results in a net stress decrease, which tends to stabilize the forearc and causes low values of Λ , despite the concomitant stress reversal (Figure 2j). The stabilizing effect of the stress decrease reflects that the forearc must sustain much higher stresses before than after the earthquake, which makes postseismic failure unlikely. The effect of the stress decrease is also not counterbalanced by an increase in τ along the strengthening megathrust segment, which has a small impact on the stress in the inner forearc only. Consequently, only a narrow range of preseismic and postseismic stress states leads to an increase in Λ across the forearc.

3. Model Application to Japan and Discussion of Results

We apply our approach to Japan using finite-element models that account for margin topography, crustal thickness, water load, slab morphology, and extent of the seismogenic megathrust along the Sendai and Iwaki transects shown in Figure 1. We adjust the preseismic and postseismic μ' values of the weakening and strengthening megathrust segments until the following conditions are fulfilled: first, the bulk of aftershocks and seismic moment release occurs in areas of increased failure tendency. Second, the postseismic stress state is consistent with the prevailing fault kinematics in the forearc after the Tohoku earthquake (Figure 1d). These conditions are fulfilled for the preseismic and postseismic stress states shown in Figures 3a and 3b (Figure S3 in Supporting Information S1). The modeled stress change (Figure 3c) causes a failure tendency increase over large areas that encompass $\sim 98\%$ of the aftershocks and seismic moment release, while all normal faulting occurs in areas under deviatoric tension (Figures 3d and 3e). For comparison, slightly different preseismic and postseismic stress states are incompatible with the observed aftershock distribution and fault kinematics (Figures S4 and S5 in Supporting Information S1).

The modeled megathrust stress drop is spatially heterogeneous and differs for the Sendai and Iwaki transects (Figure 3c). The largest decrease in megathrust shear stress occurs at shallow and intermediate depth along the Sendai and Iwaki transects, respectively, resembling spatial differences in fault slip (Figure 1b). The stress drop along the weakening and strengthening fault segments varies between 18 and -12 MPa, respectively. The net stress drop averaged over the Sendai and Iwaki transects is ~ 2 MPa. The modeled stress drop is comparable to independent stress-drop estimates from 40 different slip-distribution models that vary between 30 and -20 MPa and yield a rupture-zone average < 5 MPa (Brown et al., 2015; Wang et al., 2019). The megathrust stress drop in our models relates to changes in μ' along the weakening and strengthening segments of < 0.02 (Figures 3a and 3b). The preseismic μ' values of the seismogenic megathrust vary between 0.02 and 0.025, in good agreement with previous estimates of ~ 0.02 – 0.03 derived from heat dissipation and force-balance models (Gao & Wang, 2014; Lamb, 2006; Seno, 2009; Wang et al., 2019).

The stress drop causes changes in deviatoric stress (σ_{dev}) from -10 to 20 MPa in the forearc (Figure 3c), while absolute values of σ_{dev} vary between 5 and 60 MPa both for the preseismic and postseismic model steps (Figures 3a

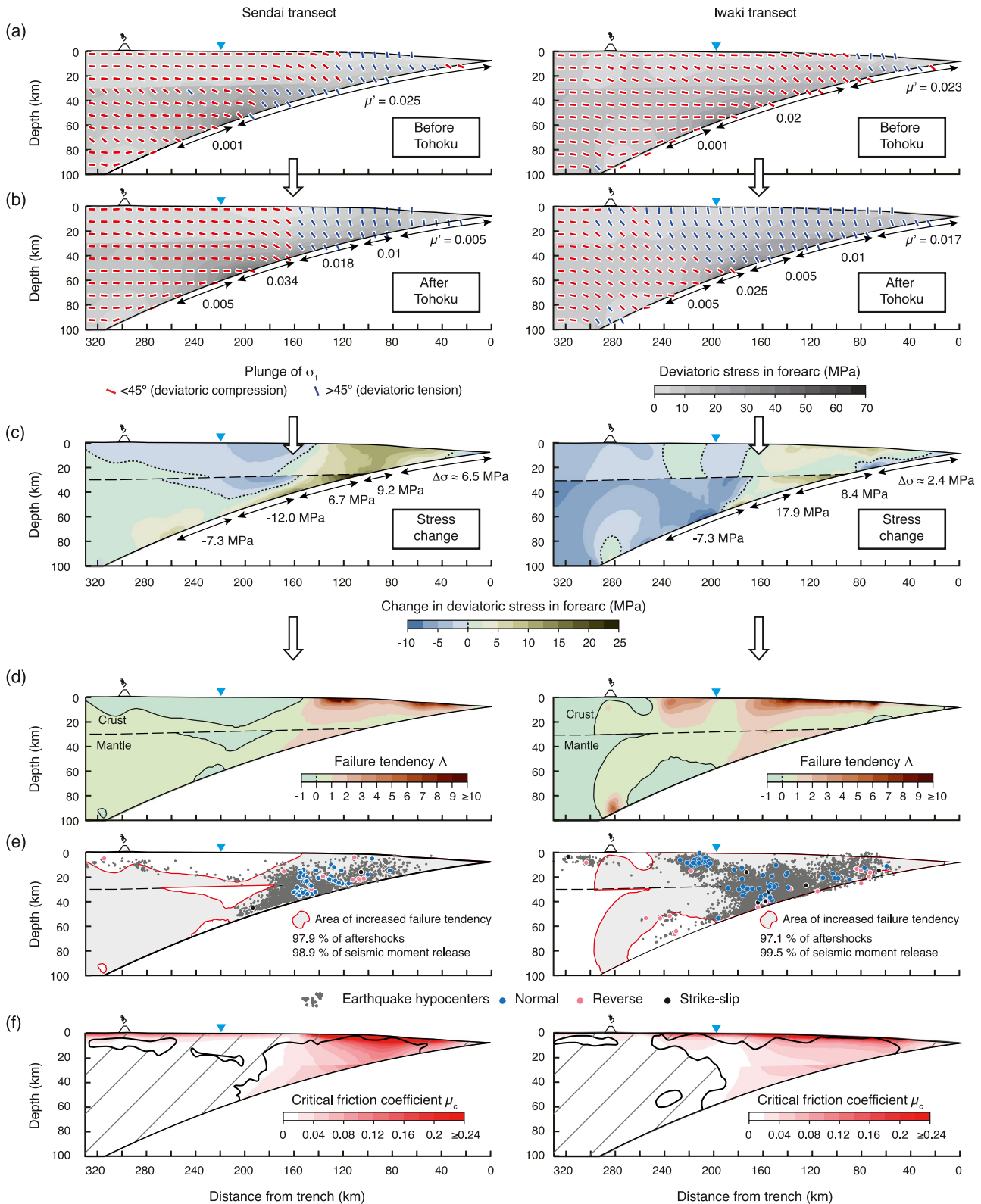


Figure 3. Model results for Japan. (a, b) Deviatoric stress and plunge of σ_1 for preseismic and postseismic model steps. (c) Change in σ_{dev} in the forearc due to megathrust stress drop $\Delta\sigma$. Positive and negative values of $\Delta\sigma$ indicate decrease and increase in megathrust shear stress, respectively. (d, e) Failure tendency Λ . Gray dots and red, blue, and black solid circles in (e) are hypocenters of forearc seismicity and reverse, normal, and strike-slip faulting events after the Tohoku earthquake, respectively (see Figure 1d). (f) Critical friction coefficient $\mu_{c,post}$ which estimates the effective strength of faults in areas showing aftershock seismicity. Hatched areas indicate areas showing no seismicity, for which fault strength cannot be estimated.

and 3b). Megathrust stress drop, σ_{dev} , and change in σ_{dev} have the same order of magnitude, in agreement with previous estimates derived from stress reversals in the marine forearc (Hardebeck, 2012; Hasegawa et al., 2011). Furthermore, we find that the stress drop does not result in a general forearc stress decrease, but also in local stress increases. Interestingly, $\sim 78\%$ of the aftershock seismicity and $\sim 92\%$ of the seismic moment release occur in areas in which σ_{dev} increases (Tables S2 and S3 in Supporting Information S1). The areas lie within areas of increased failure tendency and encompass the marine forearc and coastal region near Iwaki (Figures 3b–3d). The megathrust stress drop and gravitational stresses arising from steep forearc topography control the σ_{dev} increase, particularly in the marine forearc. The topographic effect near Iwaki, however, is due to a local topographic high along the coast, the Abukuma plateau—a feature that is missing near Sendai (Figure S1b in Supporting Information S1). Our models, therefore, indicate that differences in forearc topography together with spatial stress drop differences have a discernible impact on forearc stress changes and likely facilitated the differences in coastal aftershock seismicity along strike of the forearc (Figure 1b). We also find a dearth of aftershock activity in forearc areas that experience a decrease in σ_{dev} , including inland Japan and the shelf region along the Sendai transect. Only the outermost marine forearc offshore Sendai deviates from this trend and shows little aftershock seismicity despite σ_{dev} increases.

Spatial variations in fault strength may govern spatial variability in aftershock seismicity (Wang et al., 2019). We therefore evaluate how the critical friction coefficient $\mu_{\text{c,post}}$ varies across the forearc (Figure 3f). Parameter $\mu_{\text{c,post}}$ is calculated from the postseismic stress solutions (Section 2) and is a composite parameter that includes the effects of both intrinsic friction and pore fluid pressure in the fault zone. It therefore provides an estimate for the effective strength of faults that were seismically active after the Tohoku earthquake. The effective fault strength in forearc areas showing no aftershock seismicity is likely higher than $\mu_{\text{c,post}}$ as they seem not to have failed at the given stresses.

The $\mu_{\text{c,post}}$ in the outermost forearc offshore Sendai is ~ 0.075 – 0.24 , i.e., highest in the forearc. The comparatively high strength may indicate that the outer forearc is generally stronger than more internal parts. Alternatively, the apparent strength may represent a postseismic condition and result from the large coseismic seaward displacement of the outer forearc, which exceeded 20 m above the main slip area close to the trench (Kido et al., 2011; Sato et al., 2011). The strong seaward displacement causes forearc dilation that tends to decrease pore pressures and increase fault strength (Manga et al., 2012). This interpretation is consistent with the higher seismicity in the outer forearc offshore Iwaki, where the seaward displacement was much smaller (~ 5 m) and should not lead to a similar dilational strengthening effect.

Most aftershocks in both transects occur between ~ 120 and ~ 200 km from the trench and locate in the mantle wedge and overlying crust. The associated faults are likely very weak, in accordance with $\mu_{\text{c,post}}$ values of ~ 0.01 – 0.06 (Figure 3f). The low fault strength may relate to mantle wedge serpentinization and pressure buildup from fluids liberated from the subducting slab (Hyndman & Peacock, 2003; Tulley et al., 2022). Thus, the intense seismicity in the area may be linked to the position above the dehydrating slab.

Further inland, $\mu_{\text{c,post}}$ is < 0.02 for all but the upper 5–10 km of the forearc, and suggests that inland Japan hosts weak faults and quasi-lithostatic pore fluid pressures. In contrast to the mantle-wedge setting, high pore fluid pressures are likely locally restricted because of the large distance to the dehydrating slab. The local restriction of high fluid pressures is consistent with previous studies showing that the inland seismicity is linked to hydrothermal fluid migration along mature fault systems (Okada et al., 2011; Yoshida et al., 2017). The inland seismicity was also interpreted to have been triggered by local fluid pressure increases (Terakawa et al., 2013). A pressure increase would raise the failure tendency and may explain the seismicity underneath the volcanic arc not captured in our model (Figure 3e). Nevertheless, the low inland seismicity may be conditioned by very low background stresses that are marginally capable of initiating frictional failure, suggesting that these regions deform mainly viscously. Similar conditions will also apply to mantle areas that show very low or no seismic activity, although the failure tendency partially increases (Figures 3d and 3e).

4. Comparison of Model Stresses With Static Stress Drop of Forearc Earthquakes

Our models constrain the preseismic and postseismic stresses in the Japanese forearc. We now validate the stress solutions independently by comparison with static stress-drop estimates of earthquakes that occurred in the forearc before and after the Tohoku earthquake (Figure 4a). Earthquake stress drop magnitudes are restricted

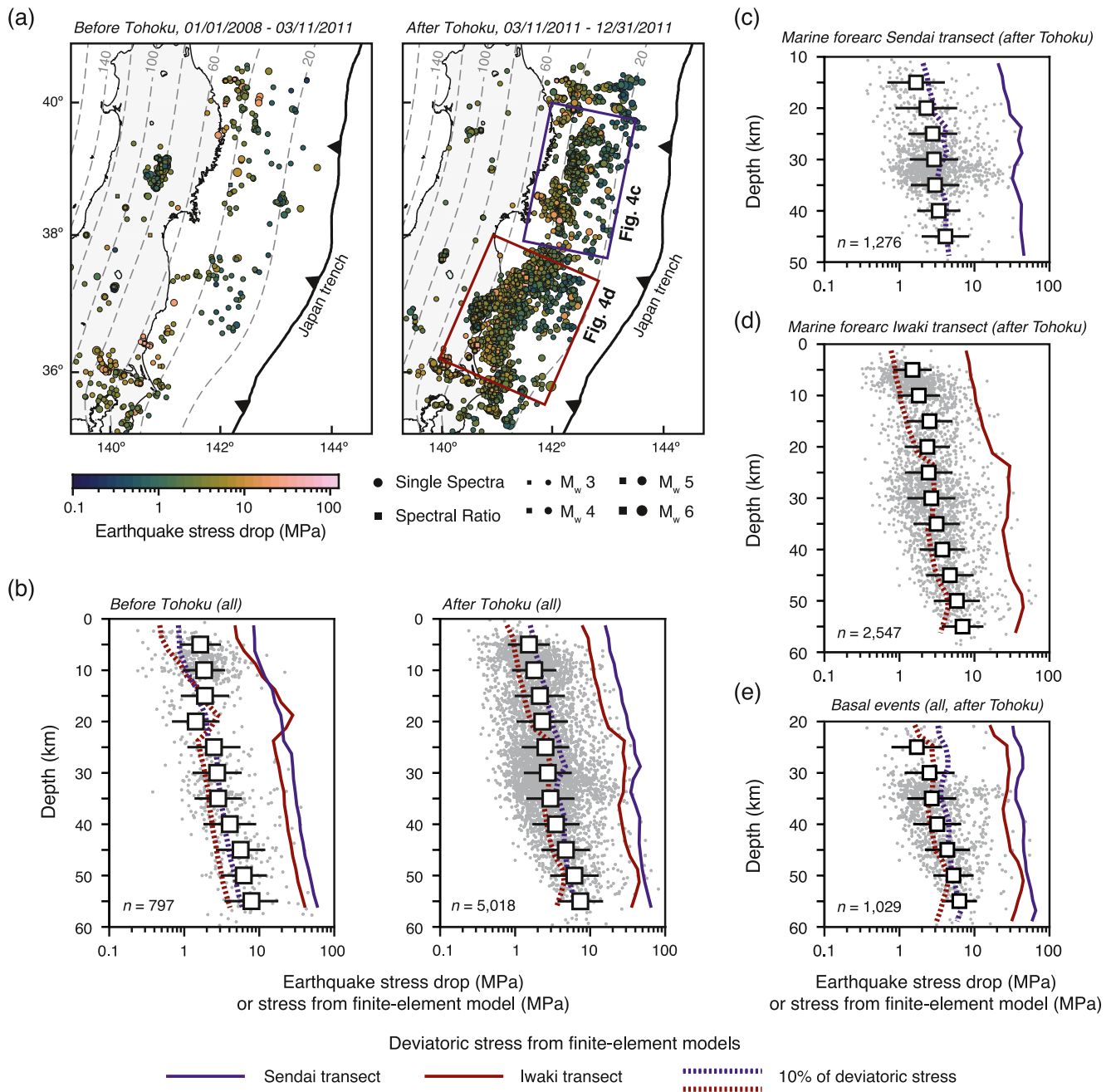


Figure 4. Earthquake stress drop values and comparison to model stresses (solid and dashed lines in c–e). (a, b) Earthquake hypocenters with estimated static stress drop. (c–e) Gray dots are individual stress-drop estimates (n = total number of estimates), squares are average stress drop values ($\overline{\Delta\sigma}_{\text{Forearc}}$). Error bars represent one standard deviation. Basal events in (e) are events from 1 to 5 km above the slab interface.

by the stress along the fault that ruptured and provide a lower bound for deviatoric stress derived from the finite-element models. In addition, spatiotemporal stress drop heterogeneities may hint at variations in ambient stresses (Kemna et al., 2021).

We estimate stress drop values using seismic data from the NIED High Sensitivity Seismograph Network (National Research Institute for Earth Science and Disaster Resilience, 2019) and the Japanese Meteorological Agency (JMA). As individual stress-drop estimates may reflect local stress heterogeneities that are not representative of average stresses, we first determine individual earthquake stress drop values using both single-spectra and spectral-ratio fitting methods. We then calculate average stress drop values ($\overline{\Delta\sigma}_{\text{Forearc}}$) at 10-km depth intervals

with 50% overlap (Text S3 and S4 and Figures S8 and S9 in Supporting Information S1). The averaged values better reflect bulk stress conditions in the forearc and are better suited for comparison with modeled stresses (Moyer et al., 2020).

The pre-Tohoku and post-Tohoku $\overline{\Delta\sigma}_{\text{Forearc}}$ values are largely similar and increase gradually with depth from ~ 2 to 8 MPa (Figure 4b). The stress drop estimation incorporates a depth-dependent velocity model from the JMA, thus the observed increase with depth is not an artifact of a constant shear velocity assumption (Abercrombie et al., 2021; Hauksson, 2015). A selection of similar event pairs within 5 km hypocentral distance further ensures a depth-dependent attenuation correction for stress drop values obtained using the spectral-ratio fitting method (Abercrombie et al., 2021; Figure S10 in Supporting Information S1). Aside from the depth dependency, the $\overline{\Delta\sigma}_{\text{Forearc}}$ values are spatially homogenous and do not vary significantly along forearc strike (Figure 4a). Likewise, stress drop values vary negligibly in time without a discernible trend (Figure S11d in Supporting Information S1). The range in estimated stress drop magnitudes presented here is consistent with previous estimates for the Japanese forearc (Yoshida et al., 2017).

We compare stress-drop estimates with model results by calculating the depth-dependent maximum values of σ_{dev} from the models for the Sendai and Iwaki transects (Figure 4b) and for the subregions that include most of the aftershocks (Figures 4c–4e). The depth-dependent deviatoric stresses are similar for the preseismic and postseismic states, which reflects that the maximum stresses did not change significantly due to the modeled stress drop. Similarity in the preseismic and postseismic σ_{dev} values resemble the constancy of $\overline{\Delta\sigma}_{\text{Forearc}}$ values. Moreover, the deviatoric stresses are generally higher than the stress-drop estimates, consistent with partial stress release during earthquakes (Brune, 1970; Simpson, 2018), and exhibit a similar depth dependency to $\overline{\Delta\sigma}_{\text{Forearc}}$. The remarkably consistent correlation across the forearc follows the trend of $\overline{\Delta\sigma}_{\text{Forearc}}$ being $\sim 10\%$ of σ_{dev} (Figures 4c–4e), suggesting that the average stress release scales with ambient stress. Taken together, we find that the deviatoric stresses obtained from the finite-element models agree favorably with the $\overline{\Delta\sigma}_{\text{Forearc}}$ values obtained from seismic data and validates the significance of the modeled forearc stresses.

5. Summary and Conclusions

We examine aftershock triggering by the stress drop of a megathrust earthquake and show that triggering is only possible for a narrow range of stress drop values and preseismic forearc stresses. We determine the range of values for the aftershock seismicity of the Tohoku earthquake using numerical force-balance models that are constrained by the observed aftershock distribution and fault kinematics. The model results are consistent with major aspects of the earthquake, including the magnitude and spatial heterogeneity of the stress drop, the strength of the Japanese megathrust, and the partial stress reversal in the forearc. Our models further indicate that $\sim 78\%$ of the aftershock seismicity and $\sim 92\%$ of the seismic moment release occurred in forearc areas of net stress increase, and that the detailed aftershock distribution was also governed by spatial variability in fault strength. Finally, we find that the modeled forearc stresses are remarkably consistent with independent estimates of earthquake stress drop values in the forearc before and after the Tohoku earthquake. Given the consistency in the data and its implications, we conclude that the bulk forearc seismicity in the first months after the Tohoku earthquake was triggered by the megathrust stress drop and resulting stress change in the forearc. This stress change will not remain unchanged after the megathrust earthquake but will be altered by viscoelastic relaxation processes, and relocking and reloading of the megathrust in the years after the megathrust earthquake (Bedford et al., 2016; Bürgmann et al., 2016; Sobolev & Muldashev, 2017; Sun et al., 2014). Viscoelastic relaxation and reloading tend to diminish the failure tendency and forearc seismicity with time. Whether the observed power-law like decrease in forearc seismicity already reflects these or other processes remains to be resolved. Independently, our approach helps to determine the stress perturbation in the forearc caused by the megathrust stress drop and can be applied to other great megathrust earthquakes to obtain detailed information on forearc stress and strength.

Data Availability Statement

Waveform data from the Hi-net borehole network of the National Research Institute for Earth Science and Disaster Resilience (2019). We downloaded Hi-net waveforms using the HinetPy package, Version 0.6.9 (<https://10.5281/zenodo.4777177>). Hypocentral locations and phase arrivals for Japan are available from the Japan Meteorological Agency (<http://www.data.jma.go.jp/svd/eqev/data/bulletin/hypo.html>). Estimated stress drop values, list of

events used in this study, and ABAQUS output databases are available from <https://doi.org/10.25835/0072357>. We used the mtspec Python wrapper for spectral estimations (Prieto et al., 2009). We process seismic data and create maps, swath profiles, and diagrams using the Python packages Obspy (Krischer et al., 2015), Matplotlib (Hunter, 2007), and GMT (Wessel et al., 2019). Color schemes follow *Scientific colour maps* (Cramer et al., 2020). The finite-element models were calculated, processed, and plotted using the commercial software packages ABAQUS and MATLAB and the Matlab tool Abaqus2Matlab by Papazafeiropoulos et al. (2017).

Acknowledgments

We thank S. Takemura (ERI, Japan) and D. Tian (MSU, USA) for the helpful suggestions on downloading and processing of Hi-net data from Japan. We thank the National Research Institute for Earth Science and Disaster Resilience and the Japan Meteorological Agency for granting open access to seismological data. Reviews by Iris van Zelst and an anonymous reviewer improved the clarity of the manuscript.

References

- Abercrombie, R. E., Trugman, D. T., Shearer, P. M., Chen, X., Zhang, J., Pennington, C. N., et al. (2021). Does earthquake stress drop increase with depth in the crust? *Journal of Geophysical Research: Solid Earth*, *126*, e2021JB022314. <https://doi.org/10.1029/2021JB022314>
- Bedford, J., Moreno, M., Li, S., Oncken, O., Baez, J. C., Bevis, M., et al. (2016). Separating rapid relocking, afterslip, and viscoelastic relaxation: An application of the postseismic straightening method to the Maule 2010 cGPS. *Journal of Geophysical Research: Solid Earth*, *121*, 7618–7638. <https://doi.org/10.1002/2016JB013093>
- Brodsky, E. E., Mori, J. J., Anderson, L., Chester, F. M., Conin, M., Dunham, E. M., et al. (2020). The state of stress on the fault before, during, and after a major earthquake. *Annual Review of Earth and Planetary Sciences*, *48*(1), 49–74. <https://doi.org/10.1146/annurev-earth-053018-060507>
- Brown, L., Wang, K., & Sun, T. (2015). Static stress drop in the M_w 9 Tohoku-oki earthquake: Heterogeneous distribution and low average value. *Geophysical Research Letters*, *42*, 10595–10600. <https://doi.org/10.1002/2015GL066361>
- Brune, J. N. (1970). Tectonic stress and the spectra of seismic shear waves from earthquakes. *Journal of Geophysical Research*, *75*(26), 4997–5009. <https://doi.org/10.1029/JB075i026p04997>
- Bürgmann, R., Uchida, N., Hu, Y., & Matsuzawa, T. (2016). Tohoku rupture reloaded? *Nature Geoscience*, *9*(3), 183. <https://doi.org/10.1038/ngeo2649>
- Cramer, F., Shephard, G. E., & Heron, P. J. (2020). The misuse of colour in science communication. *Nature Communications*, *11*(1), 5444. <https://doi.org/10.1038/s41467-020-19160-7>
- Cubas, N., Avouac, J.-P., Leroy, Y. M., & Pons, A. (2013). Low friction along the high slip patch of the 2011 M_w 9.0 Tohoku-Oki earthquake required from the wedge structure and extensional splay faults. *Geophysical Research Letters*, *40*, 4231–4237. <https://doi.org/10.1002/grl.50682>
- Dewey, J. W., Choy, G., Presgrave, B., Sipkin, S., Tarr, A. C., Benz, H., et al. (2007). Seismicity associated with the Sumatra-Andaman Islands earthquake of 26 December 2004. *Bulletin of the Seismological Society of America*, *97*(1A), S25–S42. <https://doi.org/10.1785/0120050626>
- Dielforder, A. (2017). Constraining the strength of megathrusts from fault geometries and application to the Alpine collision zone. *Earth and Planetary Science Letters*, *474*, 49–58. <https://doi.org/10.1016/j.epsl.2017.06.021>
- Dielforder, A., & Hampel, A. (2021). Force-balance analysis of stress changes during the subduction-collision transition and implications for the rise of mountain belts. *Journal of Geophysical Research: Solid Earth*, *126*, e2020JB020914. <https://doi.org/10.1029/2020JB020914>
- Di Toro, G., Han, R., Hirose, T., De Paola, N., Nielsen, S., Mizoguchi, K., et al. (2011). Fault lubrication during earthquakes. *Nature*, *471*(7339), 494–498. <https://doi.org/10.1038/nature09838>
- Farfás, M., Comte, D., Roecker, S., Carrizo, D., & Pardo, M. (2011). Crustal extensional faulting triggered by the 2010 Chilean earthquake: The Pichilemu Seismic Sequence. *Tectonics*, *30*, TC6010. <https://doi.org/10.1029/2011TC002888>
- Gao, X., & Wang, K. (2014). Strength of stick-slip and creeping subduction megathrusts from heat flow observations. *Science*, *345*(6200), 1038–1041. <https://doi.org/10.1126/science.1255487>
- Hardebeck, J. L. (2012). Coseismic and postseismic stress rotations due to great subduction zone earthquakes. *Geophysical Research Letters*, *39*, L21313. <https://doi.org/10.1029/2012GL053438>
- Hasegawa, A., Yoshida, K., Asano, Y., Okada, T., Inuma, T., & Ito, Y. (2012). Change in stress field after the 2011 great Tohoku-Oki earthquake. *Earth and Planetary Science Letters*, *355–356*, 231–243. <https://doi.org/10.1016/j.epsl.2012.08.042>
- Hasegawa, A., Yoshida, K., & Okada, T. (2011). Nearly complete stress drop in the 2011 M_w 9.0 off the Pacific coast of Tohoku earthquake. *Earth Planets and Space*, *63*(7), 703–707. <https://doi.org/10.5047/eps.2011.06.007>
- Hauksson, E. (2015). Average stress drops of Southern California earthquakes in the context of crustal geophysics: Implications for fault zone healing. *Pure and Applied Geophysics*, *172*(5), 1359–1370. <https://doi.org/10.1007/s00024-014-0934-4>
- Hunter, J. D. (2007). Matplotlib: A 2D graphics environment. *Computing in Science & Engineering*, *9*(3), 90–95. <https://doi.org/10.1109/mcse.2007.55>
- Hyndman, R. D., & Peacock, S. M. (2003). Serpentinization of the forearc mantle. *Earth and Planetary Science Letters*, *212*(3–4), 417–432. [https://doi.org/10.1016/s0012-821x\(03\)00263-2](https://doi.org/10.1016/s0012-821x(03)00263-2)
- Kemna, K. B., Verdecchia, A., & Harrington, R. M. (2021). Spatio-temporal evolution of earthquake static stress drop values in the 2016–2017 central Italy seismic sequence. *Journal of Geophysical Research: Solid Earth*, *126*, e2021JB022566. <https://doi.org/10.1029/2021JB022566>
- Kido, M., Osada, Y., Fujimoto, H., Hino, R., & Ito, Y. (2011). Trench-normal variation in observed seafloor displacements associated with the 2011 Tohoku-Oki earthquake. *Geophysical Research Letters*, *38*, L24303. <https://doi.org/10.1029/2011GL050057>
- Krischer, L., Megies, T., Barsch, R., Beyreuther, M., Lecocq, T., Caudron, C., & Wassermann, J. (2015). ObsPy: A bridge for seismology into the scientific Python ecosystem. *Computational Science & Discovery*, *8*(1), 014003. <https://doi.org/10.1088/1749-4699/8/1/014003>
- Lamb, S. (2006). Shear stresses on megathrusts: Implications for mountain building behind subduction zones. *Journal of Geophysical Research*, *111*, B07401. <https://doi.org/10.1029/2005JB003916>
- Lange, D., Tilmann, F., Barrientos, S. E., Contreras-Reyes, E., Methe, P., Moreno, M., et al. (2012). Aftershock seismicity of the 27 February 2010 M_w 8.8 Maule earthquake rupture zone. *Earth and Planetary Science Letters*, *317–318*, 413–425. <https://doi.org/10.1016/j.epsl.2011.11.034>
- Manga, M., Beresnev, I., Brodsky, E. E., Elkhoury, J. E., Elsworth, D., Ingebritsen, S. E., et al. (2012). Changes in permeability caused by transient stresses: Field observations, experiments, and mechanisms. *Reviews of Geophysics*, *50*, RG2004. <https://doi.org/10.1029/2011RG000382>
- Moyer, P. A., Boettcher, M. S., Bohnenstiehl, D. R., & Abercrombie, R. E. (2020). Crustal strength variations inferred from earthquake stress drop at Axial Seamount surrounding the 2015 eruption. *Geophysical Research Letters*, *47*, e2020GL088447. <https://doi.org/10.1029/2020GL088447>
- Nakamura, W., Uchida, N., & Matsuzawa, T. (2016). Spatial distribution of the faulting types of small earthquakes around the 2011 Tohoku-oki earthquake: A comprehensive search using template events. *Journal of Geophysical Research: Solid Earth*, *121*, 2591–2607. <https://doi.org/10.1002/2015JB012584>
- National Research Institute for Earth Science and Disaster Resilience. (2019). *NIED Hi-net*. National Research Institute for Earth Science and Disaster Resilience. <https://doi.org/10.17598/NIED.0003>

- Okada, T., Yoshida, K., Ueki, S., Nakajima, J., Uchida, N., Matsuzawa, T., et al. (2011). Shallow inland earthquakes in NE Japan possibly triggered by the 2011 off the Pacific coast of Tohoku earthquake. *Earth Planets and Space*, 63(7), 749–754. <https://doi.org/10.5047/eps.2011.06.027>
- Papazafeiropoulos, G., Muñoz-Calvente, M., & Martínez-Pañeda, E. (2017). Abaqus2Matlab: A suitable tool for finite element post-processing. *Advances in Engineering Software*, 105, 9–16. <https://doi.org/10.1016/j.advengsoft.2017.01.006>
- Parsons, T. (2002). Global Omori law decay of triggered earthquakes: Large aftershocks outside the classical aftershock zone. *Journal of Geophysical Research*, 107(B9), 2199. <https://doi.org/10.1029/2001JB000646>
- Prieto, G. A., Parker, R. L., & Vernon, F. L. (2009). A Fortran 90 library for multitaper spectrum analysis. *Computers & Geosciences*, 35(8), 1701–1710. <https://doi.org/10.1016/j.cageo.2008.06.007>
- Sato, M., Ishikawa, T., Ujihara, N., Yoshida, S., Fujita, M., Mochizuki, M., & Asada, A. (2011). Displacement above the hypocenter of the 2011 Tohoku-Oki earthquake. *Science*, 332(6036), 1395. <https://doi.org/10.1126/science.1207401>
- Scholz, C. H. (1998). Earthquakes and friction laws. *Nature*, 391(6662), 37–42. <https://doi.org/10.1038/34097>
- Seno, T. (2009). Determination of the pore fluid pressure ration at seismogenic megathrusts in subduction zones: Implications for strength of asperities and Andean-type mountain building. *Journal of Geophysical Research*, 114, B05404. <https://doi.org/10.1029/2008JB005889>
- Sibson, R. H. (1998). Brittle failure mode plots for compressional and extensional tectonic regimes. *Journal of Structural Geology*, 20(5), 655–660. [https://doi.org/10.1016/s0191-8141\(98\)00116-3](https://doi.org/10.1016/s0191-8141(98)00116-3)
- Simpson, G. (2018). What do earthquakes reveal about ambient shear stresses in the upper crust? *Geology*, 46(8), 703–706. <https://doi.org/10.1130/G45052.1>
- Sobolev, S. V., & Muldashev, I. A. (2017). Modeling seismic cycles of great megathrust earthquakes across the scales with focus at postseismic phase. *Geochemistry, Geophysics, Geosystems*, 18, 4387–4408. <https://doi.org/10.1002/2017GC007230>
- Sun, T., Wang, K., Iinuma, T., Hino, R., He, J., Fujimoto, H., et al. (2014). Prevalence of viscoelastic relaxation after the 2011 Tohoku-oki earthquake. *Nature*, 514(7520), 84–87. <https://doi.org/10.1038/nature13778>
- Terakawa, T., Hashimoto, C., & Matsu'ura, M. (2013). Changes in seismic activity following the 2011 Tohoku-oki earthquake: Effects of pore fluid pressure. *Earth and Planetary Science Letters*, 365, 17–24. <https://doi.org/10.1016/j.epsl.2013.01.017>
- Toda, S., & Stein, R. S. (2022). Central shutdown and surrounding activation of aftershocks from megathrust earthquake stress transfer. *Nature Geoscience*, 15(6), 494–500. <https://doi.org/10.1038/s41561-022-00954-x>
- Toda, S., Stein, R. S., & Lin, J. (2011). Widespread seismicity excitation throughout central Japan following the 2011 M=9.0 Tohoku earthquake and its interpretation by Coulomb stress transfer. *Geophysical Research Letters*, 38, L00G03. <https://doi.org/10.1029/2011GL047834>
- Tulley, C. J., Fagereng, Á., Ujiie, K., Diener, J. F. A., & Harris, C. (2022). Embrittlement within viscous shear zones across the base of the subduction thrust seismogenic zone. *Geochemistry, Geophysics, Geosystems*, 23, e2021GC010208. <https://doi.org/10.1029/2021GC010208>
- van Zelst, I., Wollherr, S., Gabriel, A.-A., Madden, E. H., & van Dinther, Y. (2019). Modeling megathrust earthquakes across scales: One-way coupling from geodynamics and seismic cycles to dynamic rupture. *Journal of Geophysical Research: Solid Earth*, 124, 11414–11446. <https://doi.org/10.1029/2019JB017539>
- Wang, K., Brown, L., Hu, Y., Yoshida, K., He, J., & Sun, T. (2019). Stable forearc stressed by a weak megathrust: Mechanical and geodynamic implications of stress changes caused by the M = 9 Tohoku-Oki earthquake. *Journal of Geophysical Research: Solid Earth*, 124, 6179–6194. <https://doi.org/10.1029/2018JB017043>
- Wang, K., & He, J. (1999). Mechanics of low stress forearcs: Nankai and Cascadia. *Journal of Geophysical Research*, 104(B7), 15191–15205. <https://doi.org/10.1029/1999JB900103>
- Wessel, P., Luis, J. F., Uieda, L., Scharroo, R., Wobbe, F., Smith, W. H. F., & Tian, D. (2019). The generic mapping tools version 6. *Geochemistry, Geophysics, Geosystems*, 20, 5556–5564. <https://doi.org/10.1029/2019GC008515>
- Yang, Y. R., Johnson, K. M., & Chuang, R. Y. (2013). Inversion for absolute deviatoric crustal stress using focal mechanisms and coseismic stress changes: The 2011 M9 Tohoku-oki, Japan, earthquake. *Journal of Geophysical Research: Solid Earth*, 118, 5516–5529. <https://doi.org/10.1002/jgrb.50389>
- Yoshida, K., Hasegawa, A., Okada, T., Iinuma, T., Ito, Y., & Asano, Y. (2012). Stress before and after the 2011 great Tohoku-oki earthquake and induced earthquakes in inland areas of eastern Japan. *Geophysical Research Letters*, 39, L03302. <https://doi.org/10.1029/2011GL049729>
- Yoshida, K., Hasegawa, A., Yoshida, T., & Matsuzawa, T. (2019). Heterogeneities in stress and strength in Tohoku and its relationship with earthquake sequences triggered by the 2011 M9 Tohoku-oki Earthquake. *Pure and Applied Geophysics*, 176(3), 1335–1355. <https://doi.org/10.1007/s00024-018-2073-9>
- Yoshida, K., Saito, T., Urata, Y., Asano, Y., & Hasegawa, A. (2017). Temporal changes in stress drop, frictional strength, and earthquake size distribution in the 2011 Yamagata-Fukushima, NE Japan, earthquake swarm, caused by fluid migration. *Journal of Geophysical Research: Solid Earth*, 122, 10379–10397. <https://doi.org/10.1002/2017JB014334>

References From the Supporting Information

- Abercrombie, R. E. (2021). Resolution and uncertainties in estimates of earthquake stress drop and energy release. *Philosophical Transactions of the Royal Society A: Mathematical, Physical & Engineering Sciences*, 379(2196), 20200131. <https://doi.org/10.1098/rsta.2020.0131>
- Amante, C., & Eakins, B. W. (2009). ETOPO1 1 Arc-Minute Global Relief model NOAA Technical Memorandum. <https://doi.org/10.7289/V5C8276M>
- Bakun, W. H., & Bufe, C. G. (1975). Shear-wave attenuation along the San Andreas fault zone in central California. *Bulletin of the Seismological Society of America*, 65(2), 439–459. <https://doi.org/10.1785/bssa0650020439>
- Boatwright, J. (1980). A spectral theory for circular seismic sources; simple estimates of source dimension, dynamic stress drop, and radiated seismic energy. *Bulletin of the Seismological Society of America*, 70(1), 1–27.
- Cailleau, B., & Oncken, O. (2008). Past forearc deformation in Nicaragua and coupling at the megathrust interface: Evidence for subduction retreat? *Geochemistry, Geophysics, Geosystems*, 9, Q03016. <https://doi.org/10.1029/2007GC001754>
- Erdős, Z., Huismans, R. S., Faccenna, C., & Wolf, S. G. (2021). The role of subduction interface and upper plate strength on back-arc extension: Application to Mediterranean back-arc basins. *Tectonics*, 40, e2021TC006795. <https://doi.org/10.1029/2021TC006795>
- Eshelby, J. D. (1957). The determination of the elastic field of an ellipsoidal inclusion, and related problems. *Proceedings of the Royal Society of London Series A*, 241, 376–396. <https://doi.org/10.1098/rspa.1957.0133>
- Hampel, A., Lüke, J., Krause, T., & Hetzel, R. (2019). Finite-element modeling of glacial isostatic adjustment (GIA): Use of elastic foundations at material boundaries versus the geometrically non-linear formulation. *Computers & Geosciences*, 122, 1–14. <https://doi.org/10.1016/j.cageo.2018.08.002>

- Hanks, T. C., & Kanamori, H. (1979). A moment magnitude scale. *Journal of Geophysical Research*, 84(B5), 2348–2350. <https://doi.org/10.1029/JB084iB05p02348>
- Hayes, G. P., Moore, G. L., Portner, D. E., Hearne, M., Flamme, H., Furtney, M., & Smoczyk, G. M. (2018). Slab2, A comprehensive subduction zone geometry model. *Science*, 362(6410), 58–61. <https://doi.org/10.1126/science.aat4723>
- Ide, S., Beroza, G. C., Prejean, S. G., & Ellsworth, W. L. (2003). Apparent break in earthquake scaling due to path and site effects on deep borehole recordings. *Journal of Geophysical Research*, 108(B5), 2271. <https://doi.org/10.1029/2001JB001617>
- Iwasaki, T., Levin, V., Nikulin, A., & Iidaka, T. (2013). Constraints on the Moho in Japan and Kamchatka. *Tectonophysics*, 609, 184–201. <https://doi.org/10.1016/j.tecto.2012.11.023>
- Kanamori, H., & Anderson, D. L. (1975). Theoretical basis of some empirical relations in seismology. *Bulletin of the Seismological Society of America*, 65(5), 1073–1095.
- Kaneko, Y., & Shearer, P. M. (2015). Variability of seismic source spectra, estimated stress drop, and radiated energy, derived from cohesive-zone models of symmetrical and asymmetrical circular and elliptical ruptures. *Journal of Geophysical Research: Solid Earth*, 120, 1053–1079. <https://doi.org/10.1002/2014JB011642>
- Madariaga, R. (1976). Dynamics of an expanding circular fault. *Bulletin of the Seismological Society of America*, 66(3), 639–666. <https://doi.org/10.1785/bssa0660030639>
- Maeda, T., Obara, K., Furumura, T., & Saito, T. (2011). Interference of long-period seismic wavefield observed by the dense Hi-net array in Japan. *Journal of Geophysical Research*, 116, B10303. <https://doi.org/10.1029/2011JB008464>
- Newville, M., Stensitzki, T., Allen, D. B., Rawlik, M., Ingargiola, A., & Nelson, A. (2016). Lmfit: Non-linear least-square minimization and curve-fitting for Python. *Astrophysics Source Code Library ascl: 1606.014*.
- Obara, K., Kasahara, K., Hori, S., & Okada, Y. (2005). A densely distributed high-sensitivity seismograph network in Japan: Hi-net by National Research Institute for Earth Science and Disaster Prevention. *Review of Scientific Instruments*, 76(2), 021301. <https://doi.org/10.1063/1.1854197>
- Pacor, F., Gallović, F., Puglia, R., Luzi, L., & D'Amico, M. (2016). Diminishing high-frequency directivity due to a source effect: Empirical evidence from small earthquakes in the Abruzzo region, Italy. *Geophysical Research Letters*, 43, 5000–5008. <https://doi.org/10.1002/2016GL068546>
- Prieto, G. A., Parker, R. L., Vernon, F. L., Shearer, P. M., & Thomson, D. J. (2006). Uncertainties in earthquake source spectrum estimation using empirical green functions. In R. Abercrombie, A. McGarr, G. Di Toro, & H. Kanamori (Eds.), *Earthquakes: Radiated energy and the physics of faulting*. <https://doi.org/10.1029/170GM08>
- Schwanghart, W., & Scherler, D. (2014). TopoToolbox 2—MATLAB-based software for topographic analysis and modeling in Earth surface sciences. *Earth Surface Dynamics*, 2, 1–7. <https://doi.org/10.5194/esurf-2-1-2014>
- Thomson, D. J. (1982). Spectrum estimation and harmonic analysis. *Proceedings of the IEEE*, 70(9), 1055–1096. <https://doi.org/10.1109/proc.1982.12433>
- Wada, I., & Wang, K. (2009). Common depth of slab-mantle decoupling: Reconciling diversity and uniformity of subduction zones. *Geochemistry, Geophysics, Geosystems*, 10, Q10009. <https://doi.org/10.1029/2009GC002570>

Megathrust Stress Drop as Trigger of Aftershock Seismicity: Insights From the 2011 Tohoku Earthquake, Japan

A. Dielforder¹, G. M. Bocchini², K. Kemna², A. Hampel¹, R. M. Harrington², O. Oncken³

¹Institut für Geologie, Leibniz Universität Hannover, Germany

²Institut für Geologie, Mineralogie und Geophysik, Ruhr-Universität Bochum, Germany

³GFZ Deutsches GeoForschungsZentrum Potsdam, Germany

Contents of this file

Text S1 to S4
Figures S1 to S11
Tables S1 to S3

Introduction

Text S1 to S4 provide information on the methods used in this study. Figures S1 to S7 provide information on the finite-element models and model results not shown in the main manuscript. Figures S8 to S11 provide information on the stress drop estimation and stress drop data not shown in the main manuscript. Table S1 provides details on the frictional contact in the finite-element models for Japan. Tables S2 and S3 compare the aftershock distribution and seismic moment release, respectively, with results of the finite-element models.

Text S1. Finite-Element Model

To calculate the stress in the forearc, we use a plane-strain finite-element model of an elastic upper plate and a rigid lower plate in frictional contact following earlier studies (Dielforder & Hampel, 2021; Wang & He, 1999; Wang et al., 2019). The models are created and calculated using the commercial software ABAQUS (version 6.14). The basic model setup, boundary conditions, and material parameters are shown in Figure S1. All models are meshed using linear triangular elements with an average element edge length of ~ 2 km.

ABAQUS computes the total stress in the elastic upper plate, which results from all applied boundary conditions, including gravity, isostasy, and friction along the plate interface (Figure S1a). The gravitational force is calculated for a gravitational acceleration $g = 9.81 \text{ m s}^{-2}$ and densities of $2,800$ and $3,300 \text{ kg m}^{-3}$ for crustal and mantle parts, respectively. Seawater load is modeled using a pressure boundary condition, with values determined from seawater density ($1,025 \text{ kg m}^{-3}$) and depth. Friction is calculated for standard Coulomb friction by displacing the lower plate, such that the shear stress along the contact τ depends on friction coefficient μ' and normal stress σ_n ($\tau = \mu' \sigma_n$). Using the friction law allows us to describe the shear stress along the megathrust in a consistent manner. Still, it should be noted that after the earthquake the actual shear stress can be somewhat lower than the one predicted by the friction law.

Basal drag at the base of the lithosphere of the upper plate is not considered in our model, because basal drag is thought to have a small impact on forearc stresses only (e.g., Erdös et al., 2021). As the upper plate is elastic, it has no yield criterion and deforms only elastically, but not permanently due to plastic or viscous deformation. The model calculates no pore fluid pressures and no effective stresses (total stress minus pore fluid pressure).

At the beginning of each model run, isostatic equilibrium is established following the procedure described in Hampel et al. (2019). Afterwards, the model calculates the total stress in the forearc for a preseismic and a postseismic model step. The model steps differ by the μ' values assigned to the frictional contact. The preseismic and postseismic μ' values and resultant megathrust shear stresses are representative for the strength of the megathrust just before and after the megathrust earthquake (cf. Wang et al., 2019). Strengthening and reloading of the megathrust in the postseismic and interseismic periods is not modelled.

The frictional contact comprises three sections that represent different parts of the plate interface as illustrated in Figure S1 and outlined in the following. The upper section of the interface represents the seismogenic megathrust and comprises weakening and strengthening segments to allow for a coseismic decrease and increase in shear stress, respectively. The extent of the respective megathrust segments and their preseismic and postseismic μ' values are variable.

The middle section of the interface represents the upper part of the viscous plate interface, directly downdip of the seismogenic megathrust, where the plate-interface rheology transitions into viscous creep in nature. The stress along the viscous plate interface depends on temperature and strain rate. In the late interseismic period, the strain rate diminishes and the shear stress is low (cf. Wang et al., 2019). During the earthquake, the strain rate and the shear stress increase (e.g., Brown et al., 2015). To account for the low preseismic shear stress and the coseismic stress increase, we assign preseismic and postseismic μ' values of 0.001 and 0.005 to the middle section of the interface.

The lowermost section of the interface represents the viscous plate interface at depth >75 km. In nature, the temperature increases significantly along the viscous plate interface at about 70 - 80 km depth due to the onset of mantle wedge flow and associated heat advection (e.g., Wada & Wang, 2009). The interface shear stress is assumed to be negligible at depth

greater than 70-80 km (e.g., Lamb, 2006). We therefore model the lowermost section of the interface frictionless ($\mu' = 0$), such that the shear stress is zero.

We construct different finite-element models for the generic forearc (Figures 2) and for the Sendai and Iwaki transects across the Japanese forearc (Figures 3). The generic forearc models include a curved plate interface with an average dip angle of 18° , a 5 km deep trench, a trench-coast distance of 125 km, a maximum elevation of 1 km in the volcanic arc area at 250 to 270 km distance from the trench, and a 30-km-thick crust that thickens underneath the area of high elevation to isostatically support the topography. The forearc setup is representative for the average of global ocean-continent subduction zones (see Table 1 in Dielforder & Hampel, 2021). Note that in Figure S2e-h, we present alternative generic models for a flat forearc wedge to illustrate the gravitational effect of margin topography.

The generic forearc models are used to illustrate how 1) the deviatoric stress in the forearc and plunge of σ_1 vary with μ' and τ (stress paths in Figures 2b and S2b and f), and 2) the failure tendency Λ varies for different pairs of pre- and postseismic μ' values (Figure 2c-j). For the calculation of the stress paths, the upper interface section encompasses the upper 50 km and the model is solved for μ' values between 0 and 0.12 that apply to the entire upper interface section. Strengthening along the middle interface section is not considered and the μ' value of the middle section is always 0.001. For the calculation of the failure tendency Λ , the upper interface section encompasses the upper 40 km and the μ' values of the upper and middle interface section are varied to model weakening and strengthening behavior as indicated in Figure 2c-f.

The models for the Sendai and Iwaki transects account for the site-specific forearc topography, seawater load, interface geometry, and crustal thickness. The forearc topography is approximated by the mean elevation (Figure S1b), that we calculated along 100-km-wide swath profiles from the ETOPO1 global relief model using TopoToolbox for MATLAB (Amante & Eakins, 2009; Schwanghart & Scherler, 2014). The swath profiles run parallel to those shown in Figure 1. The interface geometry has been adopted from the Slab2 model (Hayes et al., 2018) by fitting an arc with constant curvature through the upper 100 km of the slab model (e.g., Cailleau & Oncken, 2008; Wang et al., 2019). The crust is 25 km thick at the Moho-megathrust intersection and thickens to 30 km inland Japan (Iwasaki et al., 2013). The upper interface section extends down to ~58 km depth, in accordance with a downdip limit of the seismogenic megathrust in Japan at about 55-60 km depth (e.g., Hayes et al., 2018; Gao & Wang, 2014).

The models for Japan allow weakening and strengthening along the upper interface section in accordance with stress-drop distribution models (e.g., Brown et al., 2015). The extent of the weakening and strengthening fault segments and the associated μ' values are listed in Table S1. Both the extent of the fault segments and the μ' values have been obtained during the fitting process, in which we determined the forearc stress change that best explains the observed aftershock distribution (as illustrated in Figure 3). Using a finer segmentation (for example, one segment every 5 km), does not improve the model fit. Using less segments (for example, only one or two) diminishes the fit.

Text S2. Calculation of failure tendency

The finite-element models compute the total stress in the forearc for a preseismic and postseismic model step that represent the time before and after the megathrust earthquake, respectively. The coseismic stress change is the difference in total stress between the two model steps. To evaluate whether the stress change supports or inhibits frictional failure in the forearc, we first determine from the model results the critical friction coefficient μ_c . Parameter

μ_c is indicative for the maximum effective strength of cohesionless faults that can slip at a given stress (Figure S6a). Hence, μ_c can be expressed analogous to the effective friction coefficient, that is,

$$\mu_c = \mu(1 - \lambda) = \mu \left(1 - \frac{P_f}{\sigma_z}\right), \quad (1)$$

where μ is the coefficient of friction and λ is the pore fluid pressure ratio, that is, the ratio of pore fluid pressure P_f to lithostatic stress σ_z . While the lithostatic stress is given by the results of the finite-element models, the pore fluid pressure is not given but obtained by rearranging the Coulomb criterion for a cohesionless fault $\tau = \mu(\sigma_n - P_f)$, that is,

$$P_f = (\mu\sigma_n - \tau)/\mu, \quad (2)$$

where τ is the shear stress and σ_n is the normal stress on the fault (Sibson, 1998). The shear stress is calculated from the model solutions for planes optimally oriented for failure with respect to the maximum compressive stress σ_1 as

$$\tau = 0.5(\sigma_1 - \sigma_3) \sin 2\theta, \quad (3)$$

where σ_3 is the minimum compressive stress and θ is the angle between σ_1 and the failure planes (Sibson, 1998). The principal stresses σ_1 and σ_3 are given by the results of the finite element models. Angle θ is

$$\theta = 0.5 \tan^{-1}(1/\mu). \quad (4)$$

The normal stress is calculated as

$$\sigma_n = 0.5(\sigma_1 + \sigma_3) - 0.5(\sigma_1 - \sigma_3) \cos 2\theta \quad (5)$$

Combining equations 1 and 2 gives

$$\mu_c = \mu \left(1 - \frac{\sigma_n}{\sigma_z} + \frac{\tau}{\mu\sigma_z}\right). \quad (6)$$

Based on equations 1-6, the critical friction coefficient is calculated for the stress solutions of the preseismic ($\mu_{c,pre}$) and postseismic ($\mu_{c,post}$) model steps. Comparing the μ_c values for the two model steps indicates whether the stress change supports or inhibits failure. If $\mu_{c,post} > \mu_{c,pre}$, then the postseismic stress can cause failure on stronger faults than the preseismic stress, and the stress change supports failure in the forearc (Figure S6b). Conversely, if $\mu_{c,post} < \mu_{c,pre}$, then the preseismic stress was more favorable for failure and the stress change inhibits failure (Figure S6d). Accordingly, the failure tendency can be defined as

$$\Lambda = (\mu_{c,post} - \mu_{c,pre})/\mu_{c,pre}. \quad (7)$$

Based on equations 1-7, we calculate Λ for each point in the forearc. We use $\mu = 0.7$ for all calculations. Using lower and higher values for μ slightly decreases and increases the value Λ , respectively, but has no impact on our findings and conclusions (Figure S7).

Text S3. Earthquake catalogue

We obtain hypocentral solutions and P and S phase arrivals from the Japan Meteorological Agency (JMA) (https://www.data.jma.go.jp/svd/eqev/data/bulletin/index_e.html). We consider events occurring at depths shallower than 1 km above the top of the slab (Hayes et al., 2018) to limit the amount of interplate and intraslab events in the final dataset. We further restrict the dataset of forearc events by using only high-quality hypocentral solutions, as described in the following. We consider earthquakes that occurred between the 01/01/2008 and the 12/31/2011, with JMA magnitude of $M_{JMA} \geq 2.5$, with vertical errors ≤ 5 km, and latitude and longitude errors $\leq 0.025^\circ$. The filtered catalogue consists of 21,665 events (Figure 1a) with an average latitude error of $0.005 \pm 0.003^\circ$ ($\sim 0.5 \pm 0.3$ km), an average longitude error of $0.01 \pm 0.006^\circ$ ($\sim 1 \pm 0.6$ km), and an average vertical error of 1.5 ± 0.9 km. The filtered catalogue has a magnitude of completeness (M_c) of 3.4 ± 0.3 .

Text S4. Static stress drop estimates

We use the catalogue of forearc events described in Text S3 for static stress drop calculations (e.g., Abercrombie, 2021; Kanamori & Anderson, 1975) from single spectra and spectral ratio fitting methods (Figure S8a). We estimate the displacement spectral amplitude using Thomson's multitaper method (Thomson, 1982) from S-wave windows starting 0.2 seconds before the arrival and containing 90%, 80%, and 70% of the energy at a specific station within a hypocentral distance of 25 km, 25-50 km, and ≥ 50 km, respectively (Pacor et al., 2016) (Figure S8b). We ensure that each spectrum has a signal-to-noise ratio (SNR) ≥ 3 in a magnitude-dependent frequency band (Figure S8c-d). We define the frequency band for a particular event by calculating corner frequencies corresponding to theoretical stress drop values of 0.01 and 1000 MPa, which we use as lower and upper-frequency limits, respectively. We then fit the spectra (single spectra fitting) using a trust-region-reflective minimization algorithm following Newville et al. (2016)

$$\Omega_t(f) = \frac{\Omega_0 e^{-(\pi f t / Q)}}{[1 + (f / f_c)^{2n}]^{1/\gamma}} \quad (8)$$

where Ω_0 is the long-period spectral amplitude, f is the spectral frequency, t is the travel time, Q is the quality factor, f_c is the corner frequency, and n is the high-frequency falloff rate (Boatwright, 1980; Brune, 1970). We use a spectral shape constant γ of 2 (Boatwright-model), which fits most of the spectra. We then calculate the seismic moment (M_0) using the fitted Ω_0 values as

$$M_0 = \frac{4\pi\rho c^3 R \Omega_0}{U_{\phi\theta}} \quad (9)$$

where ρ is the density, c is the S-wave velocity at the depth of the hypocenter, R is the station-event hypocentral distance, and $U_{\phi\theta}$ is the mean radiation pattern for S-waves (Madariaga, 1976). We use S-wave velocities at the hypocentral depth taken from the JMA velocity model (https://www.data.jma.go.jp/svd/eqev/data/bulletin/catalog/appendix/trtime/trt_e.html). We then calculate mean values and 95% confidence intervals for a particular event using a delete-one jackknife-mean (Prieto et al., 2006) when at least five M_0 and f_c S-wave estimates are available.

Non-source related terms such as site and path effects can bias the estimates of f_c and final stress drop. To ensure accurate estimates of f_c , we also use a spectral ratio approach. The ratio between two co-located event spectra at a specific station cancels possible site and path effects and allows high-quality f_c estimates from one or both events in the pair depending on the frequency range of high SNR (Bakun & Bufe, 1975) (Figure S8a-c). To obtain event pairs, we cross-correlate 3-component full waveforms of events within 5 km hypocentral distance and retain event pairs with a cross-correlation coefficient ≥ 0.7 and a magnitude difference ≥ 0.5 . An 0.5 magnitude difference ensures the selection of event pairs with f_c values with a resolvable difference in the spectral ratio fitting. The displacement spectral ratio $\Omega_r(f)$ between the two event spectra can be written as

$$\Omega_r(f) = \Omega_{0r} \left[\frac{1 + (f / f_{c2})^{2n}}{1 + (f / f_{c1})^{2n}} \right]^{1/\gamma} \quad (10)$$

Where f_{c1} and f_{c2} are the corner frequencies of the larger magnitude target and the smaller magnitude empirical Green's function events (eGf), respectively. The spectral shape constant γ is set to 2. We require at least five S-wave station ratios for individual event pairs, manually review the spectral ratio fits to ensure high quality, and check whether f_{c1} and f_{c2} , or only f_{c1} values are resolvable (Figure S8e).

We use M_0 values from single spectra and f_c values either from single spectra or spectral ratio analysis to calculate stress drop values ($\Delta\sigma$) assuming a circular crack model with radius $r = k\beta/f_c$ as (Eshelby, 1957)

$$\Delta\sigma = \frac{7}{16} \frac{M_0}{r^3} \quad (11)$$

where β is the shear wave velocity at the hypocentral depth and k is a constant set to 0.26 assuming a symmetrical circular model with a rupture velocity of 0.8β (Kaneko & Shearer, 2015).

We use event waveforms from the High-Sensitivity Seismograph Network of Japan (Hi-net) (Obara et al., 2005) available from the National Research Institute for Earth Science and Disaster Resilience (NIED, 2019). We downloaded waveforms from a total of 259 Hi-net stations (Figure S9a). In case of events with $M_{JMA} \geq 3.5$, we deconvolve short-period Hi-net velocity records by their seismometer response to simulate seismic waves recorded with broadband seismometers (Maeda et al., 2011) and estimate earthquake source parameters.

We calculate moment magnitudes (M_w) (Hanks & Kanamori, 1979) using the M_0 values from S-wave single spectra and observe a good fitting with respect to the magnitude values reported in the initial catalogues (Figure S9d). We do not consider events with $M_w \leq 3$ as we observe a systematic trend of lower stress drop values for these events which are likely related to observational constraints. The trend of lower stress drops for lower magnitudes ($f_c \sim 10$ -15 Hz) has commonly been related to decreasing SNR values with magnitude and frequency and to bandwidth limitations of the 100 Hz seismometers (Ide et al., 2003). We compare the corner frequency values of events for which both single spectra and spectral ratio estimates are available and find good agreement between them (Figure S9b). The good agreement between single and spectral ratio fitting estimates, together with the good spatial sampling of spectral ratio estimates (Figure S9a), ensures a high quality of the single spectra estimates. In case of events for which we obtain both spectral estimates, we associate the stress drop value obtained with the spectral ratio fitting to the event.

We obtain 5,819 stress drop estimates, including 5,458 from single spectra fitting and 361 from spectral ratio fitting (Figure S9c). The average values of Q and n are 1,121 and 2.5, respectively.

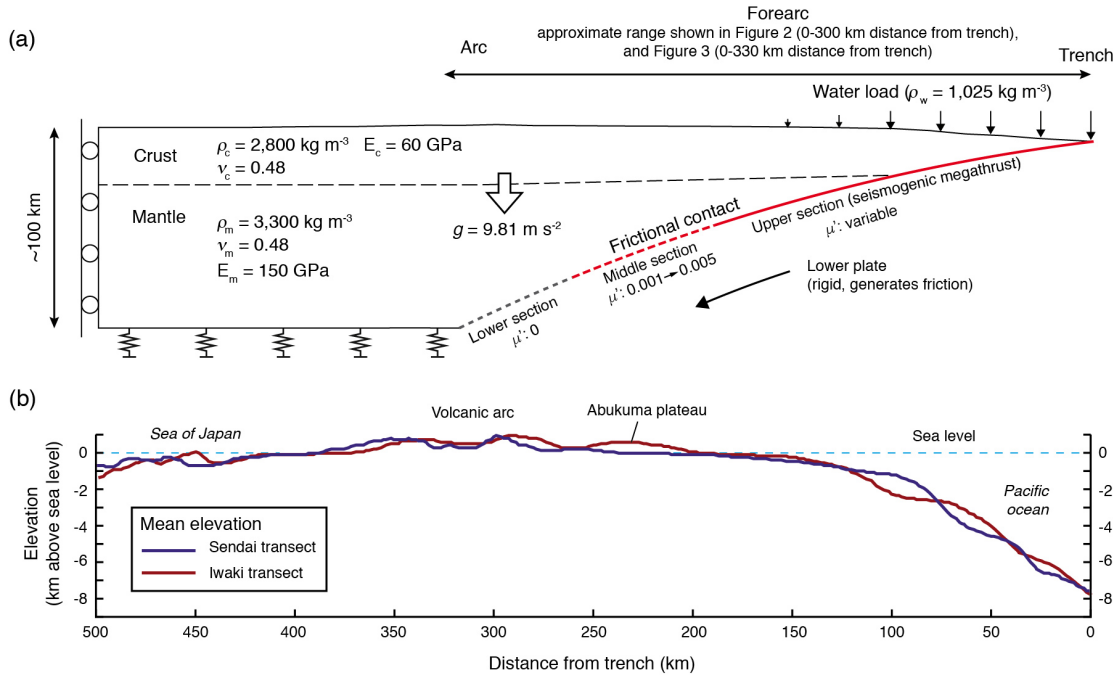


Figure S1. Model setup and forearc topography. (a) Sketch illustrating the basic setup of the finite-element model with an elastic upper plate and a rigid lower plate in frictional contact. Here g is gravitational acceleration, ρ is density, ν is Poisson ratio, E is Young's modulus, and μ' is the effective friction coefficient. The model is isostatically supported by an elastic foundation at the base of the upper plate. The left model side may move vertically and is set 500 km from the trench, that is, farther than shown in Figures 2 and 3, to minimize boundary effects. Following previous studies (Dielforder & Hampel, 2021; Wang & He, 1999; Wang et al., 2019), we adopted an almost incompressible material ($\nu = 0.48$) for the upper plate. Note that using a lower Poisson ratio (e.g., $\nu = 0.3$) has a negligible effect on the stresses only (Dielforder & Hampel, 2021). The lower plate is modeled rigid, because its role is simply generating shear stress along the frictional contact. (b) Mean elevation along 100-km-swath profiles running parallel to the Sendai and Iwaki transects shown in Figure 1. The mean elevation is used to approximate the forearc topography in the finite-element models for Japan.

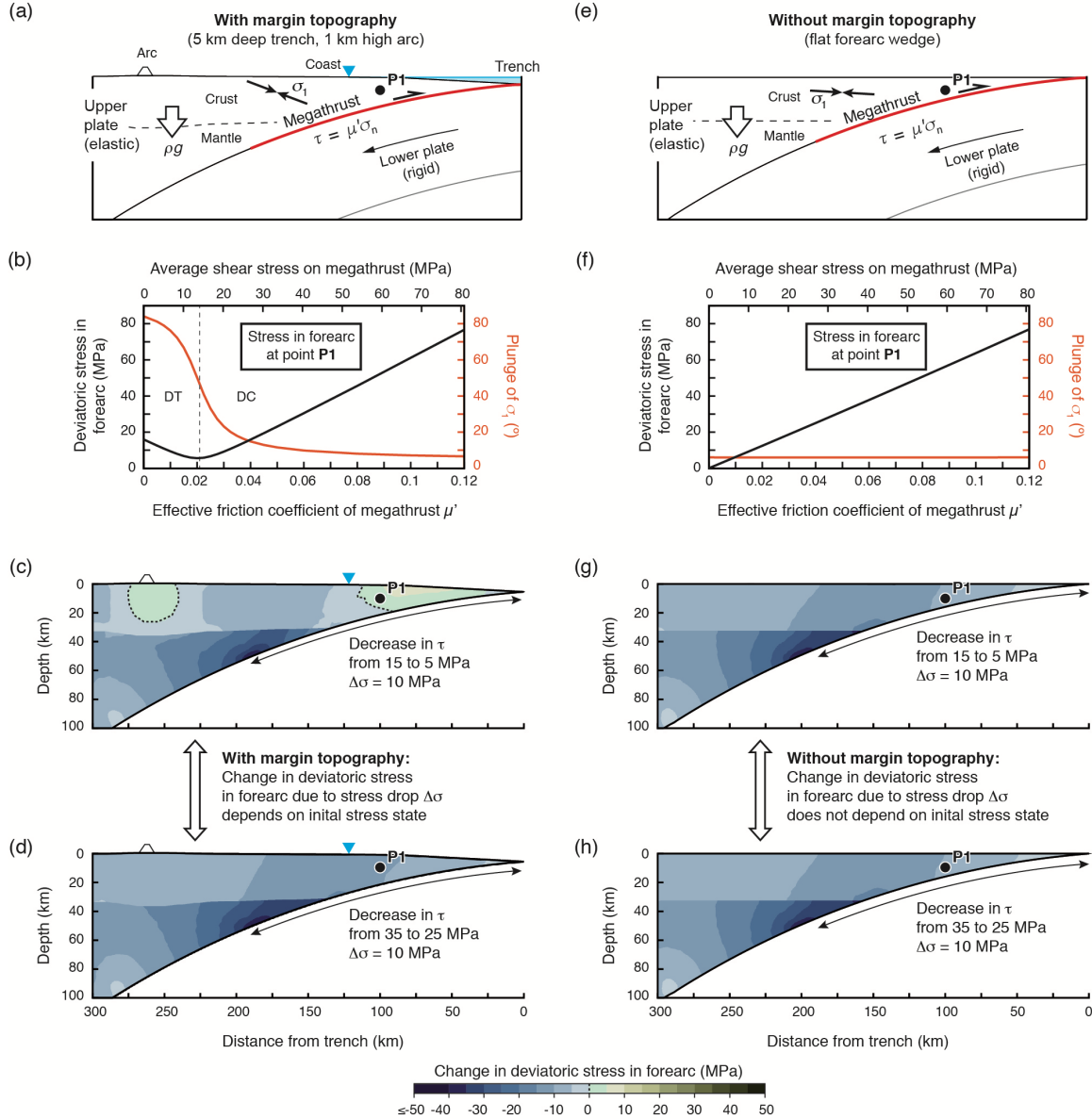


Figure S2. Dependency of forearc stress change on initial stress state. Subfigures (a) and (b) are similar to Figure 2a, b in the main text. Here ρ is density, g is gravitational acceleration, μ' is the megathrust effective friction coefficient, τ and σ_n are the shear and normal stresses, respectively, and σ_1 is maximum compressive stress. DT and DC denote deviatoric tension and deviatoric compression, respectively. (c, d) Change in deviatoric stress (σ_{dev}) in the forearc due to a decrease in average megathrust shear stress of 10 MPa from 15 to 5 MPa (c) and from 35 to 25 MPa (d). The pattern of σ_{dev} change is different for the two cases (compare c and d), because of the deviatoric tension resulting from gravity in the presence of margin topography. The gravitational effect causes that σ_{dev} and the plunge of σ_1 do not vary linearly with μ' and τ as illustrated by the stress paths in (b). Subfigures (e-h) are analogue to (a-d) but show solutions for a flat forearc wedge without margin topography. The absence of topography removes the gravitational effect and the forearc experiences no deviatoric tension. In that case, the pattern of σ_{dev} change does not depend on initial stress state (compare g and h) as σ_{dev} varies linearly with μ' and τ as illustrated by the stress path in (f).

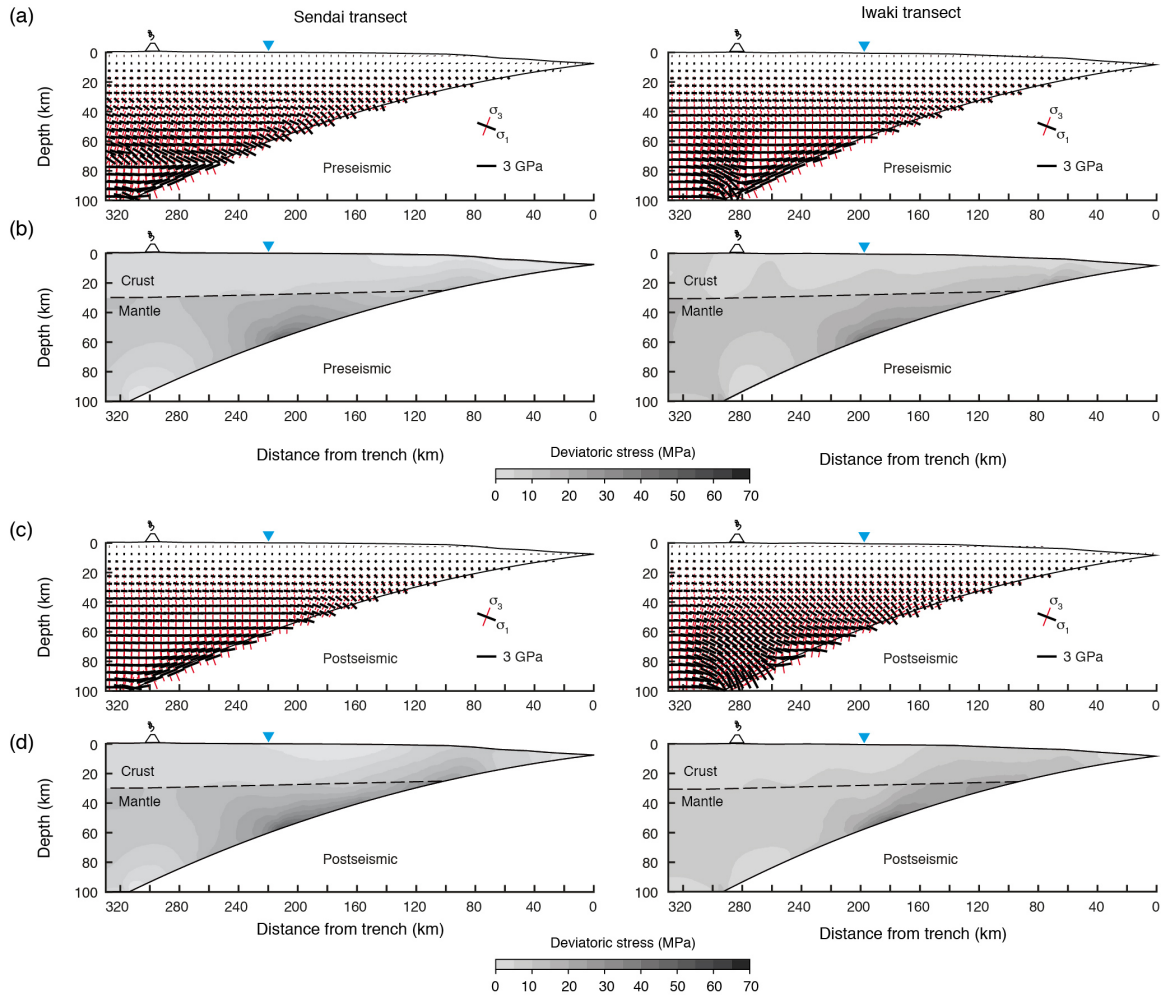


Figure S3. Model results for the Sendai and Iwaki transects, Japan. (a, c) Maximum compressive stress σ_1 (thick black bars) and minimum compressive stress σ_3 (thin red bars) for the pre-seismic (a) and post-seismic (c) model steps. Length of bars scaled. Note that the principal stresses are plotted every 5 km, while in Figure 3 σ_1 is plotted only every 10 km for reasons of illustration. (b, d) Deviatoric stress $\sigma_{dev} = 0.5(\sigma_1 - \sigma_3)$ for pre-seismic (a) and post-seismic (b) model steps. Note that the deviatoric stresses are also shown in Figure 3a and b.

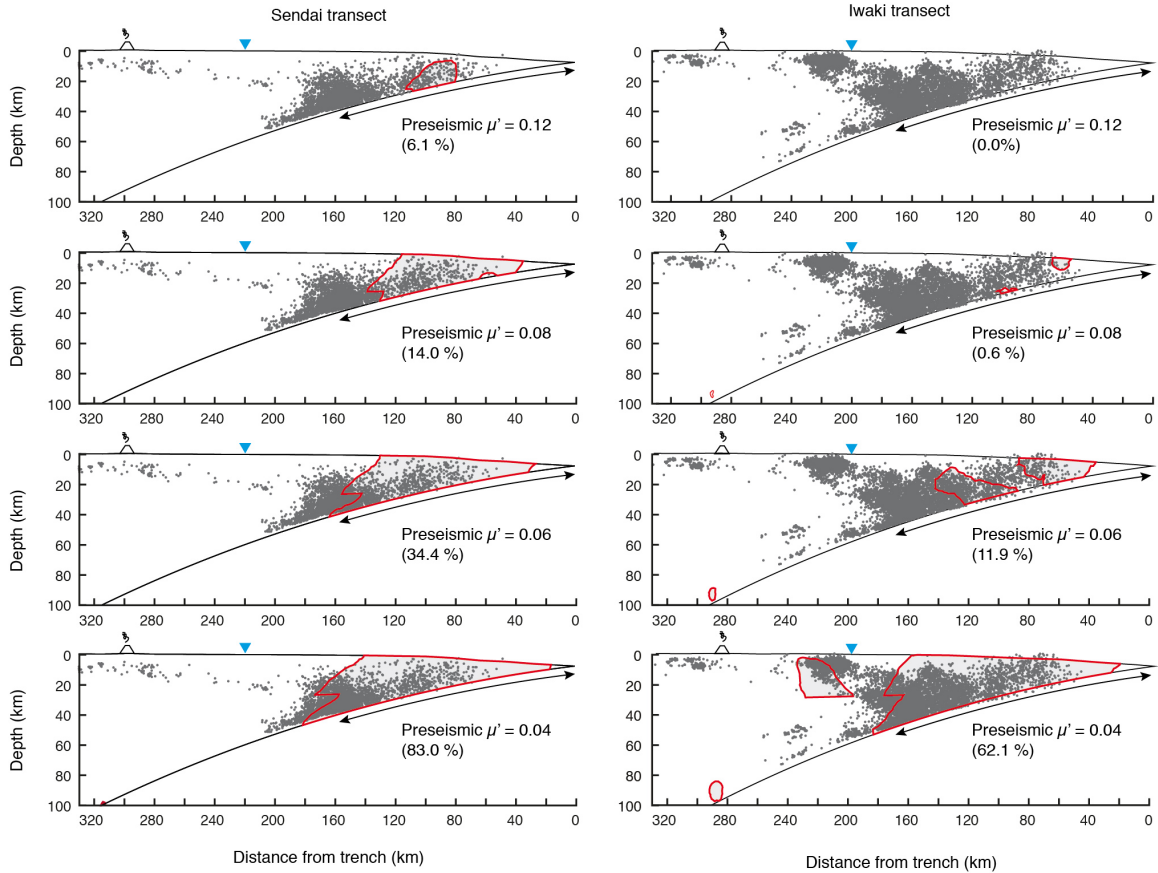


Figure S4. Set of model results illustrating the effect of the pre-seismic μ' value on failure tendency Λ . The model results are obtained from finite-element models that are identical to the models discussed in the main text but use a different μ' value for the pre-seismic model step (as indicated for each model). Gray, red-framed areas indicate forearc areas of increased failure tendency ($\Lambda > 0$) along the Sendai and Iwaki transects, Japan (compare Figure 3e). The higher the pre-seismic μ' value is, the smaller is the extent of forearc areas that experience an increase in failure tendency. The number in brackets indicates the percentage of aftershocks in areas of increased failure tendency (compare Table S2). The percentages are calculated for aftershocks with a magnitude larger or equal to the magnitude of completeness ($M_c = 3.4$).

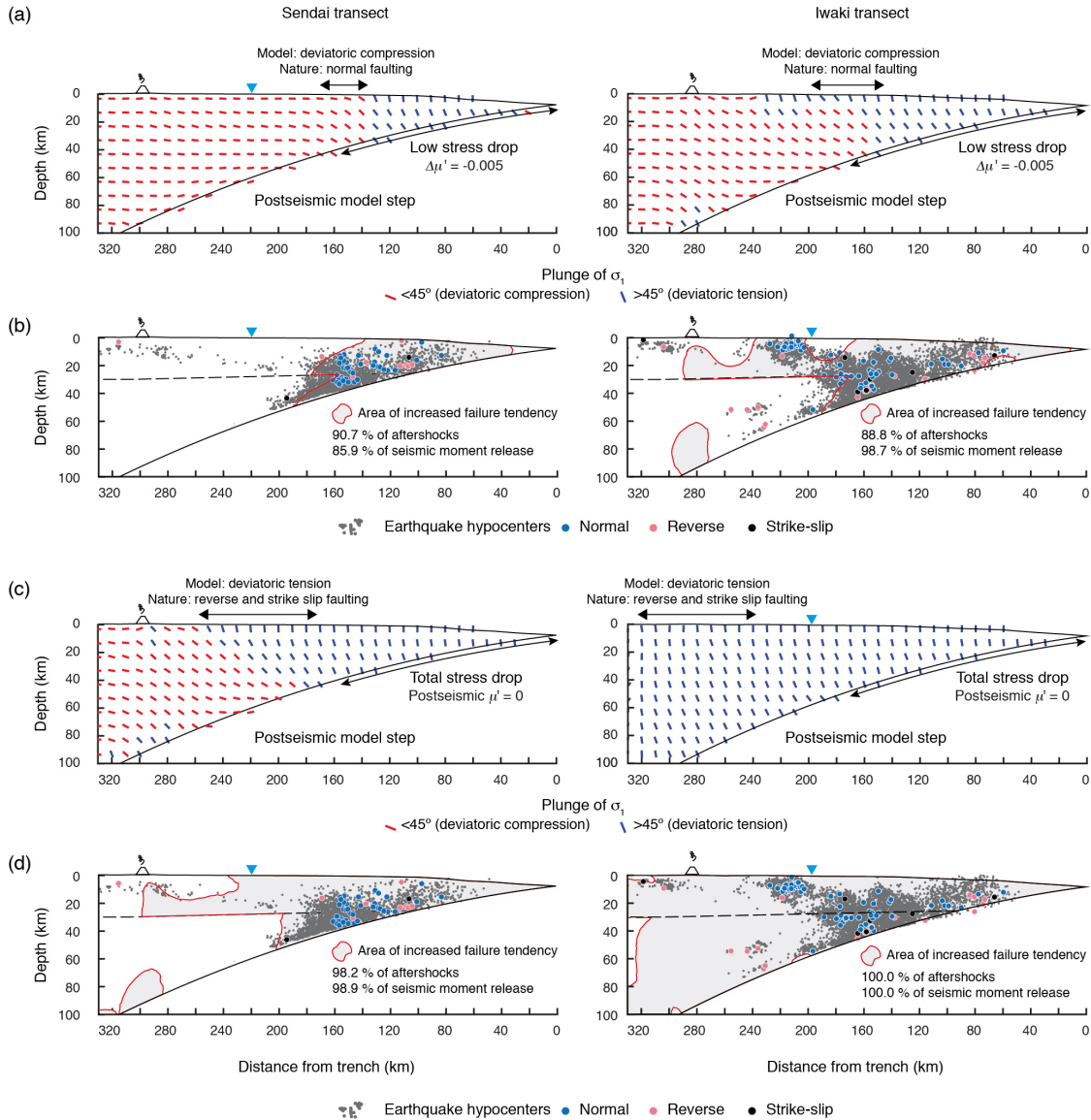


Figure S5. Set of model results illustrating the effect of the stress drop magnitude (postseismic μ' value) on the stress state (a, c) and failure tendency Δ (b, d). The model results are obtained from finite-element models that are identical to the models discussed in the main text but use a different μ' value for the postseismic model step. (a, b) Results for a low stress drop, which is modelled by decreasing μ' along the weakening segments of the megathrust by 0.005 (see Table S1 for the segmentation of the megathrust). (c, d) Results for a total stress drop, which is modelled by decreasing μ' along the weakening segments of the megathrust to zero. Both for a low (b) and total stress drop (d), most aftershocks of the Tohoku earthquake occur within areas of increased failure tendency (number in brackets in (c, d), see Figures 3 and S4 for comparison). However, the modelled stress states do not fit the observed fault kinematics in the forearc after the Tohoku earthquake. For a low stress drop (a), some forearc areas are under deviatoric compression in the model, but experienced normal faulting in nature. For a total stress drop (c), some forearc areas are under deviatoric tension in the model, but experienced reverse and strike slip faulting in nature.

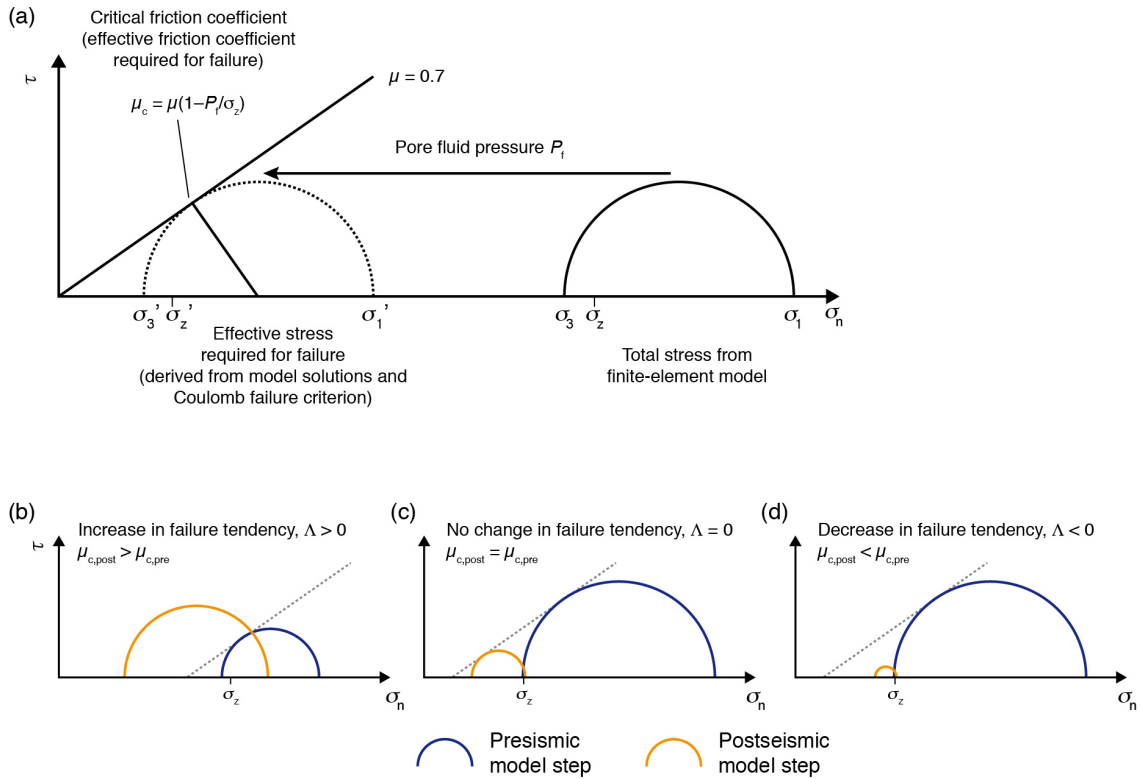


Figure S6. (a) Mohr diagram illustrating the derivation of the critical friction coefficient μ_c . See Text S2 for details. (b-d) Mohr diagrams illustrating changes in failure tendency Δ due to the stress change between the preseismic (blue) and postseismic (orange) model steps. Shown solutions are exemplary. The dashed failure envelope is shown for guidance only, but does not imply critical or unstable stress states. (b) Increase in failure tendency ($\Delta > 0$). (c) No change in failure tendency ($\Delta = 0$). (d) Decrease in failure tendency ($\Delta < 0$).

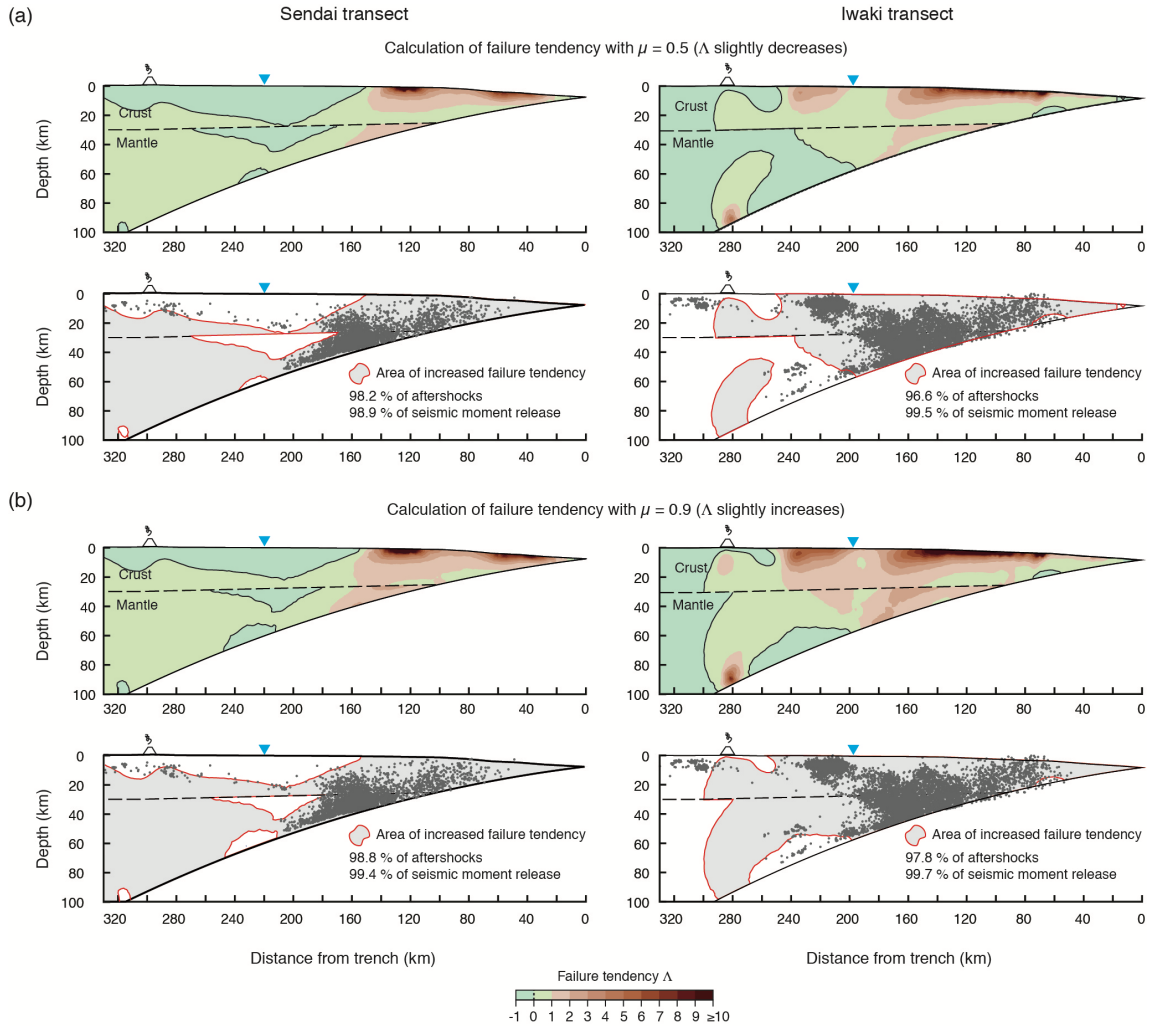


Figure S7. (a, b) Effect of friction coefficient μ (see equations 1,2, and 6 in Text S2) on failure tendency Λ . (a) Results for $\mu = 0.5$. (b) Results for $\mu = 0.9$. Note that Λ decreases and increases for lower and higher values of μ , respectively. See Figure 3d, e for comparison.

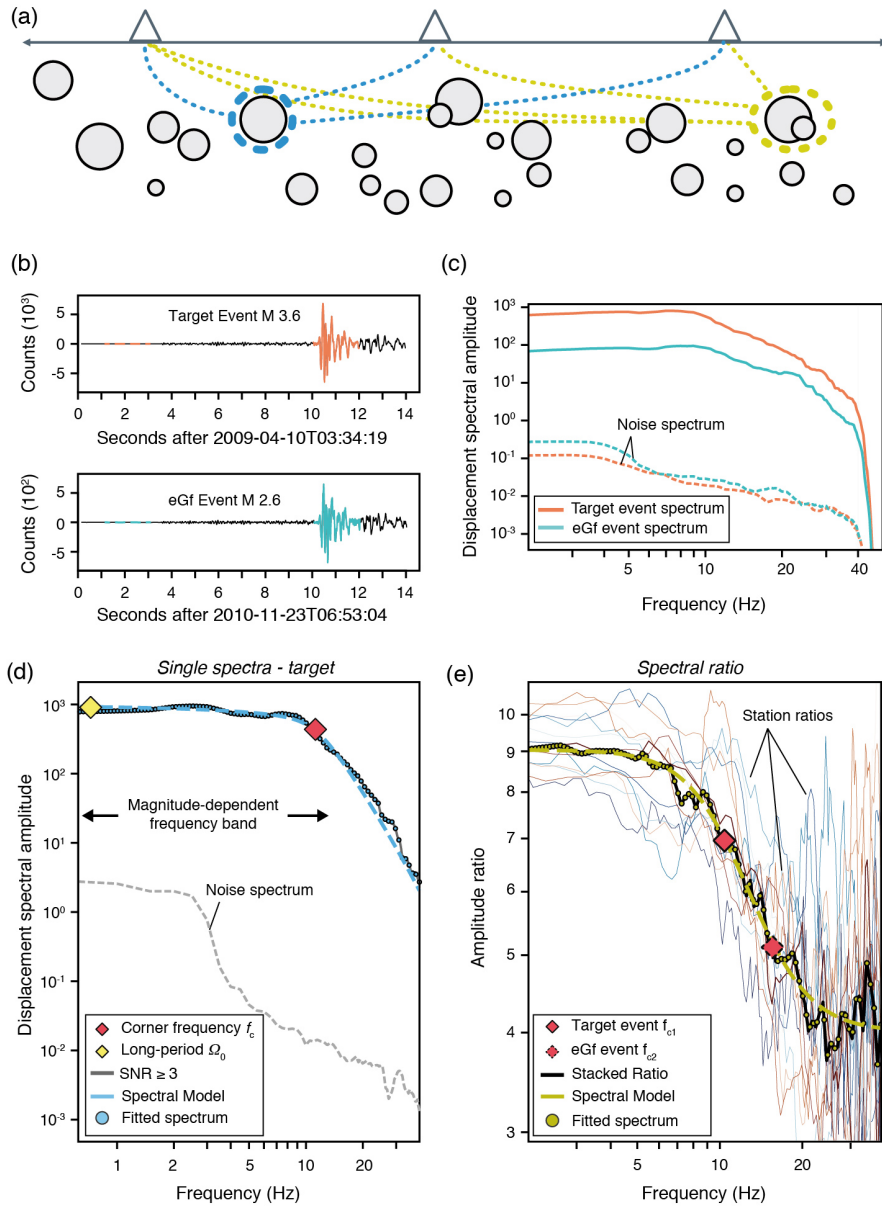


Figure S8. Single spectra and spectral ratio fitting methods. (a) Schematic representation of single spectra and spectral ratio fitting methods. Gray circles are earthquake hypocenters (scaled by magnitude), white triangles are seismic stations, and dashed lines are source-station ray paths. The blue- and yellow-colored dashed circles denote the respective crustal source volumes considered in a single iteration of single-spectrum and spectral-ratio fitting, respectively. (b) Waveform recordings of a spectral ratio event pair for the Japanese dataset with cross-correlation (CC)=0.90 at station KZMH.E from the Hi-net network. Dashed and solid lines denote the time windows for signal and noise estimation, respectively. eGf, empirical Green's function. (c) S-wave single spectra estimates for the windows shown in (b). (d) Fitted S-wave spectrum for the target event spectrum shown in (c). (e) Fitted S-wave spectral ratio from the spectra shown in (c).

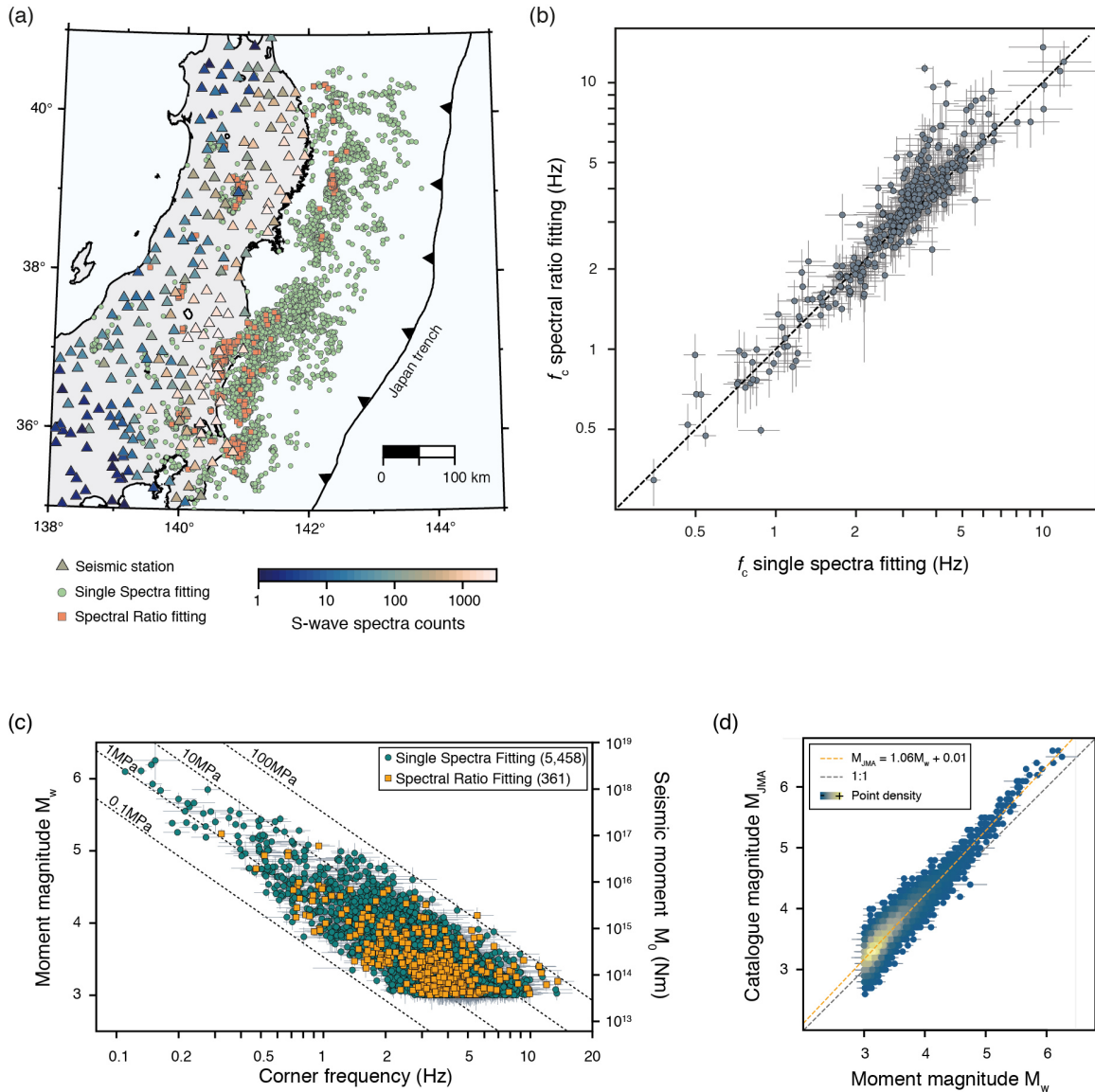


Figure S9. Single spectra and spectral ratio fitting estimates, and comparison of original and calculated magnitudes. (a) Number of S-wave spectral estimate per seismic station and distribution of single spectra and spectral ratio stress drop estimates. (b) Comparison between corner frequencies (f_c) obtained from single spectra and spectral ratio fitting methods. (c) Corner frequency with respect to moment magnitude (M_w). Green circles and orange squares indicate single spectra and spectral ratio estimates, respectively. The number in brackets gives the total number of estimates. The dashed lines denote stress-drop isolines for a shear-wave velocity of $3,400 \text{ m s}^{-1}$ at a depth range between 7 and 20 km. (d) Comparison between original magnitude of the Japanese Meteorological Agency magnitude (M_{JMA}) and calculated moment magnitudes from S-wave single spectra fitting. The dashed black line indicates a 1:1 fitting line, while the orange dashed line indicates the linear regression fitting line between original and calculated magnitudes. Error bars in (b-d) represent the 95% jackknife confidence interval.

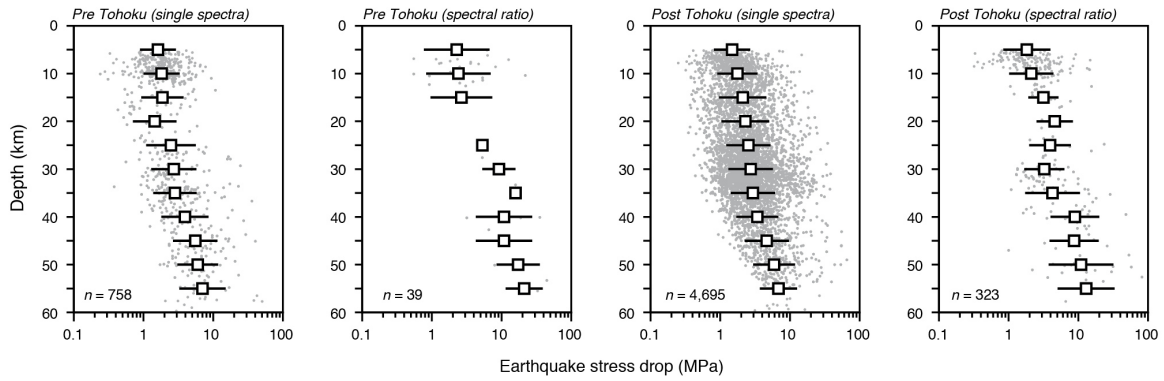


Figure S10. Comparison of stress drop values obtained from single spectra and spectral ratio fitting methods. Gray dots are individual stress-drop estimates (n = total number of estimates), squares are average stress drop values calculated at 10 km depth intervals with 50% overlap. Error bars represent one standard deviation. Note that the averages values of pre-Tohoku spectral ratio fitting estimates are statistically not representative due to the low number of estimates ($n = 39$).

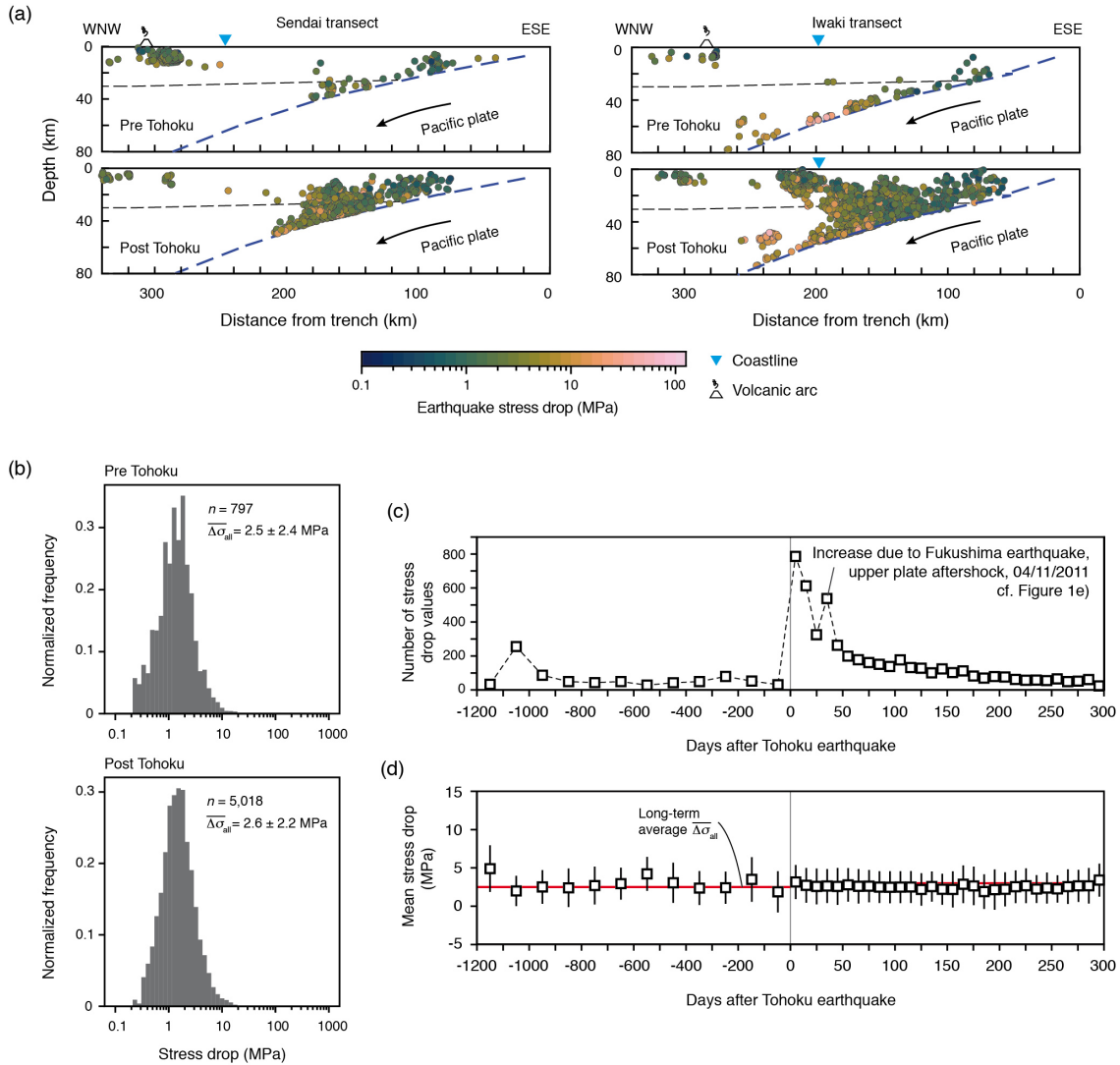


Figure S11. Static-stress-drop values of earthquakes in the Japanese forearc before (01/01/2008–03/11/2011) and after (03/11/2011–12/31/2011) the Tohoku earthquake. (a) Hypocenters of earthquakes with estimated static stress drop along the Sendai and Iwaki profiles (see Figure 1 for traces of profiles). (b) Histograms with logarithmic scale showing the log-normal distribution of all stress drops estimates of forearc earthquakes before and after the Tohoku earthquake. The $\overline{\Delta\sigma_{all}}$ values indicate the average and 1 standard deviation of all stress drop estimates. (c) Number of stress-drop values as function of time. (d) Mean stress drop values as function of time. The number of stress drop values in (c) and the mean stress drop in (d) are calculated for 100-day-intervals before the Tohoku earthquake and for 10-day-intervals after the Tohoku earthquake. The different time intervals used for the averaging in (d) consider differences in the total number of events, which is much lower for the time before the Tohoku earthquake. Error bars in (d) indicate the 1 standard deviation.

Table S1. Segmentation and properties of the frictional contact in the finite-element models for Japan, resultant megathrust shear stresses, and stress drop values

Segment depth range [km]	Segment length [km]	Weakening or strengthening (W or S)	Friction coefficient ^a μ'		Average shear stress on segment ^b [MPa]		Stress drop ^c [MPa]
			pre	post	pre	post	
<i>Sendai transect</i>							
7.7 – 10	19.3	W	0.025	0.005	1.8	0.4	1.4 ^d
10 – 20	58.8	W	0.025	0.005	8.7	1.7	7.0 ^d
20 – 25	23.8	W	0.025	0.01	15.4	6.2	9.2
25 – 40	60.4	W	0.025	0.0175	22.3	15.6	6.7
40 – 49	30.1	S	0.025	0.035	30.5	42.6	-12.1 ^e
49 – 58	28.1	S	0.025	0.033	36.6	48.3	-11.7 ^e
58 – 75	46.8	S	0.001	0.005	1.8	9.1	-7.3
<i>Iwaki transect</i>							
7.8 – 10	10.8	W	0.023	0.018	1.6	1.2	0.4 ^f
10 – 20	51.0	W	0.023	0.015	8.0	5.2	2.8 ^f
20 – 25	20.6	W	0.023	0.01	14.2	6.2	8.0 ^g
25 – 38	45.6	W	0.02	0.01	17.3	8.6	9.2 ^g
38 – 49	31.9	W	0.02	0.005	23.8	6.0	17.8
49 – 58	23.7	S	0.02	0.025	29.3	36.6	-7.3
58 – 75	40.0	S	0.001	0.005	1.8	9.1	-7.3

^aFriction coefficient μ' is a model input parameter and assigned to megathrust fault segments for the preseismic (pre) and postseismic (post) model steps.

^bThe average shear stress on the megathrust segments is an output parameter and calculated for the preseismic (pre) and postseismic (post) model steps for the respective μ' values (^a).

^cThe stress drop is an output parameter calculated by subtracting the average shear stress values (^b) for the postseismic model step from the shear stress values of the preseismic model steps. The values are illustrated in Figure 3.

^{d-g}Stress drop values marked with d, e, f, and g have been averaged for the respective megathrust segments in Figure 3 for reasons of illustration.

Table S2. Number of aftershocks

Transect	Number of aftershocks in forearc area [# , (%)]				
	Total	$\Lambda > 0^b$	$\Lambda < 0^b$	$\Delta\sigma_{dev} > 0^c$	$\Delta\sigma_{dev} < 0^c$
Sendai, all	4,708 (100)	4,551 (96.7)	157 (3.3)	4,114 (87.4)	594 (12.6)
Sendai, $M > M_c^a$	1,365 (100)	1,336 (97.9)	29 (2.1)	1,230 (90.1)	135 (9.9)
Iwaki, all	10,094 (100)	9,553 (94.6)	541 (5.4)	7,447 (73.8)	2,647 (26.2)
Iwaki, $M > M_c^a$	2,332 (100)	2,255 (97.1)	67 (2.9)	1,758 (75.7)	564 (24.3)

^aEvents with a magnitude (M) larger or equal to the magnitude of completeness ($M_c = 3.4$) only.

^bNumber of events in forearc areas, in which the failure tendency increases ($\Lambda > 0$) or decreases ($\Lambda < 0$) in the finite-element models.

^cNumber of events in forearc areas, in which the deviatoric stress σ_{dev} increases ($\Delta\sigma_{dev} > 0$) or decreases ($\Delta\sigma_{dev} < 0$) in the finite-element models.

Table S3. Seismic moment release

Transect	Seismic moment release in forearc area [10^{19} Nm, (%)] ^a				
	Total	$\Lambda > 0^c$	$\Lambda < 0^c$	$\Delta\sigma_{dev} > 0^d$	$\Delta\sigma_{dev} < 0^d$
Sendai, all	0.637 (100)	0.630 (98.8)	0.007 (1.2)	0.550 (86.4)	0.087 (13.6)
Sendai, $M > M_c^b$	0.631 (100)	0.624 (98.9)	0.007 (1.1)	0.545 (86.4)	0.086 (13.6)
Iwaki, all	2.714 (100)	2.700 (99.5)	0.014 (0.5)	2.550 (94.0)	0.164 (6.0)
Iwaki, $M > M_c^b$	2.702 (100)	2.689 (99.5)	0.013 (0.5)	2.541 (94.0)	0.161 (6.0)

^aSeismic moment release $M_0 = 10^{(1.5M_w+9.1)}$ (Hanks & Kanamori, 1979), where M_w is moment magnitude. M_w is obtained according to the empirical relationships illustrated in Figure S8d.

^bEvents with a magnitude (M) larger or equal to the magnitude of completeness ($M_c = 3.4$) only.

^cSeismic moment release in forearc areas, in which the failure tendency increases ($\Lambda > 0$) or decreases ($\Lambda < 0$) in the finite-element models.

^dSeismic moment release in forearc areas, in which the deviatoric stress σ_{dev} increases ($\Delta\sigma_{dev} > 0$) or decreases ($\Delta\sigma_{dev} < 0$) in the finite-element models.